Cytosolic Carboxypeptidase 5 maintains mammalian ependymal multicilia to ensure proper homeostasis and functions of the brain

Rubina Dad[1§], Yujuan Wang[1], Chuyu Fang[2], Yuncan Chen[1], Yuan Zhang[1], Xinwen Pan[2], Xinyue Zhang[1], Emily Swanekamp[3], Krish Patel[4], Matthias T. F. Wolf[3], Zhiguang Yuchi[1], Xueliang Zhu[2]*, and Hui-Yuan Wu[1,3]*

[1] School of Pharmaceutical Science and Technology, Tianjin University, Tianjin, 300072, China

[2] Key Laboratory of Multi-Cell Systems, Shanghai Institute of Biochemistry and Cell Biology, Center for Excellence in Molecular Cell Science, Chinese Academy of Sciences, Shanghai, 200031, China

[3] Department of Pediatrics, The University of Michigan, Ann Arbor, MI 48109, USA

[4] College of Literature, Science, and the Arts, The University of Michigan, Ann Arbor, MI 48109, USA

* Correspondence to:

Xueliang Zhu, PhD,

Key Laboratory of Multi-Cell Systems, Shanghai Institute of Biochemistry and Cell Biology,

Center for Excellence in Molecular Cell Science, Chinese Academy of Sciences,

Shanghai, 200031, China

Email: xlzhu@sibcb.ac.cn

ORCID: 0000-0001-8019-9336

Hui-Yuan Wu, PhD,

Department of Pediatrics, The University of Michigan,

8220 MSRB III, 1150 W. Medical Ctr. Dr.,

Ann Arbor, MI 48109-5646, USA

Tel: +1-(734) 615-8514

FAX: +1-(734) 763-9512

Email: huiyuanw@umich.edu

ORCID: 0000-0002-5586-8857

[§] Current address: Structure Biology Research Centre, Human Technopole, Milan, Italy

Abstract

Ependymal multicilia position at one-side on the cell surface and beat synchronously across tissue to propel the flow of cerebrospinal fluid. Loss of ependymal cilia often causes hydrocephalus. However, molecules contributing to their maintenance remain yet fully revealed. Cytosolic carboxypeptidase (CCP) family are erasers of polyglutamylation, a conserved posttranslational modification of ciliary-axoneme microtubules. CCPs possess a unique domain (N-domain) N-terminal to their carboxypeptidase (CP) domain with unclear function. Here, we show that a novel mutant mouse of *Agbl5*, the gene encoding CCP5, with deletion of its N-terminus and partial CP domain (designated *Agbl5*$^{M1/M1}$), developed lethal hydrocephalus due to degeneration of ependymal multicilia. Interestingly, multiciliogenesis was not impaired in *Agbl5*$^{M1/M1}$ ependyma. The initially formed multicilia beat at a normal frequency, but in intercellularly diverse directions, indicative of aberrant tissue-level coordination. Moreover, actin networks are severely disrupted and basal body patches are improperly displaced in mutant cells, suggesting impaired cell polarity. In contrast, *Agbl5* mutants with disruption solely in the CP domain of CCP5 (*Agbl5*$^{M2/M2}$) do not develop hydrocephalus despite increased glutamylation levels in ependymal cilia as similarly seen in *Agbl5*$^{M1/M1}$. This study revealed an unappreciated role of CCP5, particularly its N-domain, in ependymal multicilia stability associated with their polarization and coordination.

Keywords: Polyglutamylation, cytosolic carboxypeptidase, ependymal cell, multicilia, hydrocephalus,

Introduction

Ependymal cells make a single layer of epithelium that lines on the surface of cerebral ventricles. The microtubule-based multicilia formed on the apical surface of ependymal cells beat synchronously to propel the directional flow of cerebrospinal fluid (CSF). Dysfunction of ependymal multicilia is one of major causes of hydrocephalus, which is characterized by abnormal accumulation of CSF in brain ventricle system (Kundishora et al., 2021), often leading to severe neurological disorders such as seizures and mental retardation or even death (Kahle et al., 2016).

Mouse ependymal cells are born from embryonic ventricular zones during brain development and their differentiation initiates in the first postnatal week and completes around P17 (Spassky et al., 2005). Ependymal cells were differentiated from radial glia cells (RGCs) through step-wised procedures, including massive amplification of basal bodies (BBs), docking basal bodies to the apical membrane, multiciliogenesis, polarized positioning and unidirectional alignment of cilia (Lyu et al., 2024; Kyrousi et al., 2017; Ohata and Alvarez-Buylla, 2016). Cytoskeletons microtubule (MT) and filament actin play important yet distinct roles in these procedures. MTs are essential for the assembly, motility, the unidirectional alignment of cilia, and their synchronized beating across the surface of ventricles (Werner et al., 2011; Mirzadeh et al., 2010; Boutin et al., 2014; Arata et al., 2022; Lechtreck et al., 2008; Haycraft et al., 2007; Marszalek et al., 1999), while actin networks are indispensable for BB apical migration, docking (Vladar and Axelrod, 2008), polarized placement, spacing, and stability (Werner et al., 2011; Mahuzier et al., 2018). However, the molecular clues that contribute to the coordination of these multi-step procedures have not been fully revealed.

Axonemal microtubules undergo a conserved posttranslational modification (PTM)—polyglutamylation, which is processed by tubulin tyrosine ligase like (TTLL) enzymes and forms a polyglutamate side-chain attached to the γ-carboxyl of a glutamate residue in the protein primary sequence (van Dijk et al., 2007; Janke et al., 2005). Conversely, the side-chains can be erased by the 6-member cytosolic carboxypeptidase (CCP) family (Rogowski et al., 2010; Tort et al., 2014). CCP5,

encoded by *Agbl5*, is the only identified enzyme that removes the branch point γ-carboxyl linked glutamate after other CCP members shorten the side-chain (Wu et al., 2017; Rogowski et al., 2010). Polyglutamylation has recently been shown to form a specific nano-pattern along axonemal microtubules to regulate ciliary beating (Viar et al., 2023). Consistently, deregulation of axonemal glutamylation in mice results in phenotypes related to primary ciliary dyskinesia (Yang et al., 2021; Ikegami et al., 2010).

Although the prototypic CCP member Nna1/CCP1 has been primarily linked to neurodegeneration (Rogowski et al., 2010), accumulating evidence including that from analysis of the evolutionary history of CCP expressing organisms suggests the cilium- and basal body-related role of this family (Rodriguez de la Vega Otazo et al., 2013; Wang et al., 2023; He et al., 2018; Rodriguez-Calado et al., 2023). In zebrafish, knocking down CCP5 induces ciliopathic phenotypes, such as body curvature and hydrocephalus, suggesting an important role of CCP5 in ciliary motility and function (Lyons et al., 2013; Xie et al., 2022; Zhang et al., 2018). Surprisingly, *Agbl5* knockout (KO) mice with targeted disruption of the carboxypeptidase (CP) domain in CCP5 do not exhibit overt anomalies other than male infertility due to defective tail formation of developing sperm (Wu et al., 2017; Giordano et al., 2019), raising the question of its importance in mammalian epithelial motile cilia.

In addition to the CP domain, CCPs share an N-terminal domain (ND, so called N-domain) unique for this family that is folded into an antiparallel β sandwich anchored to the CP domain and contributes to the recognition of substrates (Kalinina et al., 2007; Rimsa et al., 2014; Chen et al., 2024). We and other groups reveal that CCP5 and CCP6 interact with centriolar proteins in ciliated cells (Wang et al., 2023; Rodriguez-Calado et al., 2023). In particular, CCP5 interacts with CP110 through its ND (Wang et al., 2023), indicating its role as a protein-interacting interface. It is thus possible that the previously reported *Agbl5*-deficient mice do not carry a null mutant due to their potential expression of the N-domain.

To clarify the physiological significance of CCP5, we generated a novel *Agbl5* KO allele (designated $Agbl5^{M1}$), in which the deletion was extended to the N-terminus of CCP5. Strikingly,

Agbl5$^{M1/M1}$ mice developed severe hydrocephalus and died before the age of 2 months. Interestingly, the multicilia of *Agbl5*$^{M1/M1}$ ependymal cells initially formed but underwent serious degenerations. Moreover, the initially formed multicilia in the mutant ependyma exhibit diverse intercellular beating directions and their BB patches are not properly displaced. Therefore, CCP5 is involved in intracellular positioning and intercellular coordination of mammalian ependymal multicilia that are critical for their maintenance to ensure proper homeostasis and functions of the brain.

Results

Mice carrying a null *Agbl5* mutant (*Agbl5*$^{M1/M1}$) display markedly reduced lifespan

Agbl5 KO mouse models with targeted deletion of a region encoding its carboxypeptidase domain did not exhibit overt anomaly other than male infertility (Wu et al., 2017; Giordano et al., 2019). In order to determine whether the N-domain of CCP5 possesses additional biological function, we generated a novel *Agbl5* KO allele (designated as *Agbl5*^{M1}) using CRISPR-CAS9 genome manipulation system. In this allele, the region from the start codon to intron 8, which encodes the sequence including the N-domain and part of CP domain, was replaced with a tdTomato reporter (Figure 1A). The possible off-targets were excluded by examining the top 10 possible sites predicted for each single guide RNA (sgRNA) in descendants of 2 independent founders (Table S1). The absence of *Agbl5* transcripts in the brain, eye, spinal cord, spleen, and testis of *Agbl5*^{M1M1} animals was confirmed by RT-PCR using primers targeting the region encoding the CP domain (Figure 1B).

Pregnant *Agbl5*^{M1} heterozygous females do not exhibit obvious anomaly. The *Agbl5*$^{M1/M1}$ pups appeared normal at the birth. Compared with the wild-type animals, however, *Agbl5*$^{M1/M1}$ mice showed reduced body weight between P17-P21, and stopped growth after P30 (Figure S1). At the age between P41 and P51, the homozygous mutant mice even gradually lost the weight (Figure S1). Surprisingly, unlike the previously reported *Agbl5* KO models (Wu et al., 2017; Giordano et al., 2019), *Agbl5*$^{M1/M1}$ mice hardly survive longer than 54 days (Figure 1C).

Agbl5$^{M1/M1}$ mice developed severe hydrocephalus

Upon visual inspection, we noticed that the *Agbl5*$^{M1/M1}$ mice developed dome-shaped cranium around P40 (Figure 1D-E') with a full penetration. When brains from mutants about P50 were dissected, we found that they were filled with fluid— a characteristic feature of hydrocephalus (data not shown).

Cerebrospinal fluid (CSF) is produced from choroid plexuses and fills the ventricles of the brain. It flows from the lateral ventricles (LV), through the interventricular foramens, and into the third ventricle, cerebral aqueduct, and the fourth ventricle. To assess the alteration in ventricles of *Agbl5*$^{M1/M1}$mice, serial coronal sections along the axis of the brain were microscopically examined after hematoxylin-eosin staining. Compared with those of wild-type mice (Figure 2A-C), the lateral ventricles (Figure 2D), both the dorsal and ventral 3rd ventricles (Figure 2D, D'), and the fourth ventricle (Figure 2F) of the *Agbl5*$^{M1/M1}$mutant mice were dramatically enlarged, while the aqueduct was altered to a less extent (Figure 2B, E). These results indicate that this mutation in *Agbl5* likely affects a common process required for all ventricles of brain.

We further assessed whether the hydrocephalus was caused by the blockage of the CSF flow path. The dye Evans Blue was injected into the right lateral ventricle of P30 wild-type and *Agbl5*$^{M1/M1}$ mice. An obstruction in CSF path would delay the appearance of ink in the other ventricular compartments (Zou et al., 2020). We found that for both wild-type and mutant mice, the injected dye diffused into the left lateral (Figure 2G, K), the third (Figure 2H, L), and the fourth ventricles (Figure 2J, N), suggesting a communicating hydrocephalus instead a blockage of CSF flow path in *Agbl5*$^{M1/M1}$ mice.

Ependymal multicilia in *Agbl5*$^{M1/M1}$ hydrocephalic mice are defective in both number and motility

The flow of CSF is propelled by the movement of multicilia of ependymal cells that line on the surface of ventricles. To determine the cause of hydrocephalus in *Agbl5*$^{M1/M1}$mice, the whole-mount lateral walls of lateral ventricles from P45 mice were immunostained for acetylated tubulin (Ac-tub), which is abundantly present in ciliary axoneme (Delgehyr et al., 2015). In the wild-type mice, the bundles

of Ac-tub positive multicilia evenly covered the surface of ventricle walls and their tips pointed to the same direction (Figure 3A). In contrast, Ac-tub positive multicilia bundles were sparsely detected on the ventricle walls of the mutant mice, and often with the unbundled cilia lying on the cell surface (Figure 3B). Scanning electron microscopy (SEM) analysis of lateral ventricles of P30 mice further revealed that unlike the ventricle walls of wild-type mice, which are covered with unidirectional multicilia bundles (Figure 3C, E), multicilia on the ventricle walls of mutant mice were severely lost and often with only a few cilia left in the middle of the cell surface (Figure 3D, F). These results point to the defects of multicilia in *Agbl5*$^{M1/M1}$ependymal cells.

It is possible that the loss of ependymal multicilia is secondary to other causes in *Agbl5*$^{M1/M1}$ mice. To this end, we assessed the beating patterns of the ependymal multicilia in adult mice using high-speed imaging technique. In the wild-type mice, ependymal multicilia beat unidirectionally in a synchronized pattern (Figure 3G, Movie 1). In *Agbl5* $^{M1/M1}$ependymal cells, however, the majority of remnant multicilia hardly move (Figure 3G, Movie 2), while the others beat much slower than those in wild-type, yet with each cilium in the same cluster waving with different rhythms (Movie 3). These observations suggested that in this mutant, the hydrocephalus is indeed associated with the dysfunction of ependymal cilia.

Basal bodies are largely dispersed in ependymal cells of *Agbl5*$^{M1/M1}$ hydrocephalic mice

The actin networks in ependymal cells not only contribute to the polarized placement of basal bodies (BB), but are also important to maintain their stability against the sheering force of CSF (Werner et al., 2011; Mahuzier et al., 2018; Hirota et al., 2010). We wondered whether the positioning of BBs and the integrity of actin networks were also affected in *Agbl5*$^{M1/M1}$ ependyma. Whole-mount lateral walls of the lateral ventricles (LVs) were co-stained with actin and CEP164, a distal appendage protein of BB (Graser et al., 2007). We found that unlike the wild-type ependymal cells, in which BBs were clustered at one side of cell surface and well organized in rows (Figure 3 I, J, L, M, Figure S2A), about 30% of *Agbl5*$^{M1/M1}$ ependymal cells contain dispersed BBs (Figure 3O, P, S, Figure S2B). Even in the cells with clustered BBs, the BBs were often not properly aligned (Figure 3P, R, Figure S2B), suggesting possible

defects on subapical actin network that is required for BB spacing(Mahuzier et al., 2018). Notably, in the mutant ependyma, BBs were not detected in a substantial portion of cells (Figure 3M, S).

Consistent with the observation of abnormal BB positioning in *Agbl5*$^{M1/M1}$ ependymal cells, we found that their apical actin networks, which contribute to stabilize BBs(Mahuzier et al., 2018), were severely disrupted (Figure 3N, P vs 3H, J for wild-type). Z-project images further revealed that in ependymal cells of wild-type mice, a compact apical actin patch is polarized to one side of the cell and colocalized with CEP164 immunosignals (Figure 3K-L'). In contrast, this specialized actin patch was abolished in the *Agbl5*$^{M1/M1}$ ependymal cells even around BBs that are clustered (Figure 3Q-R'). These results suggested that in *Agbl5*$^{M1/M1}$ ependymal cells, the actin networks are affected, which possibly impairs stability of BBs and their multicilia against the sheering of CSF.

Multiciliogenesis is not impaired in ependymal tissues of *Agbl5*$^{M1/M1}$ mice

Comparing the size of lateral ventricles in the wild-type and mutant mice at different postnatal stages, we found that the enlarged ventricles consistently appeared since P7 in the mutant mice (Figure S3A). Taking the advantage of the tdTomato reporter constructed in the *Agbl5*^{M1} allele, we assessed the spatial expression of *Agbl5* in the heterozygous mice. At P7, tdTomato signal was detectable in ependymal cells, but much lower in the cells in the subventricular zone (SVZ) (Figure S3B, C). At P12, tdTomato signals were highly expressed in the ependymal cell layer of all walls of LV (Figure. 4A, B), but were still largely devoid from the subventricular zone (Figure 4B, B', arrow head). In the dorsal-lateral niche of the ventricle wall, tdTomato positive cells were not restricted to the single layer on the ventricle surface, but expended a few layers laterally (Figure 4B', arrow). This spatial expression pattern supports a possible role of *Agbl5* in ependymal cell development.

Ependymal cells are born in the embryonic stages and differentiated from mono-ciliated radial glia cells (RGCs) through multiple step-wise procedures, including cell fate commitment, multiciliogenesis, and maturation (Marques et al., 2019). Their maturation predominantly takes place in the first 2 postnatal weeks (Spassky et al., 2005). We wondered whether the commitment of RGCs to the

ependymal cells fate in *Agbl5*$^{M1/M1}$ mice was affected. The expression of vimentin, a protein that marks ependymal cells since embryonic stages (Schnitzer et al., 1981; Vidovic et al., 2018) was assessed in P7 mice. It was found that cells lining along the ventricle walls of both wild-type and mutant mice were similarly positive for vimentin staining (Figure S4), suggesting that in *Agbl5*$^{M1/M1}$ mice, the commitment of RGCs to ependymal cell fate was not altered.

Foxj1 is a transcription factor that promotes the multiciliation in ependymal cells (Jacquet et al., 2009). We next determined whether the Foxj1 expression is altered in *Agbl5*$^{M1/M1}$ mice. At P7 the number of Foxj1-positive cells was increased in all three walls of lateral ventricles in *Agbl5*$^{M1/M1}$ mutants compared to that of the wild-type mice (Figure 4C-E), suggesting that the reduction of multicilia in *Agbl5*$^{M1/M1}$ ependymal cells was not caused by insufficient expression of Foxj1.

We also assessed the expression of S100β, a calcium binding protein in differentiated ependymal cells (Jacquet et al., 2009; Spassky et al., 2005; Ohata et al., 2014). At P17, almost all ependymal cells in the LV walls of wild-type mice are S100β positive (Figure 4F, G, H and Ref. (Spassky et al., 2005)). However, in *Agbl5*$^{M1/M1}$ lateral ventricles, particularly the dorsal and lateral walls, the S100β positive cells remained in a scattered pattern (Figure 4I, J, K). Interestingly, in both dorsal and lateral walls of *Agbl5*$^{M1/M1}$ LV, many cells still formed GT335 positive multicilia despite the absence of S100β expression (Figure 4J, K, arrows). The average number of S100β positive ependymal cells per length unit in the dorsal and lateral walls of mutant LV was significantly lower than that in the wild-type (Figure 4L), with that in the dorsal wall being more prominent. Taken together, in *Agbl5*$^{M1/M1}$ ependymal cells, the expression of genes promoting multiciliogenesis were not impaired but certain proteins associated with differentiated ependymal cells are not properly expressed.

Agbl5 loss leads to increased glutamylation level in the lateral ventricle

Among the 6 CCP family members, CCP5 is the only one catalyzing the removal of branch point glutamate in the modified proteins (Rogowski et al., 2010; Wu et al., 2017; Kimura et al., 2010). The

glutamylation levels in *Agbl5*$^{M1/M1}$ lateral ventricle were assessed using GT335 antibody, which recognizes the branch point glutamate (Wolff et al., 1992), and polyE antibody, which detects more than 3 glutamate residues at C-termini respectively (Figure 5A) (Rogowski et al., 2010; Lacroix et al., 2010). Similar to the other parts of the brain (Rogowski et al., 2010), tubulin glutamylation level in the lateral ventricles is low at P7, but is greatly increased at P21 and remains at a similar level at P30 (Figure 5B). Compared with wild-type mice, loss of *Agbl5* led to an increased GT335 level in the lateral ventricles of all ages examined, but did not change the immunoreactivity for polyE (Figure 5B). These results are similar to what was observed in cerebella of previously reported *Agbl5* KO mice (Wu et al., 2017), reflecting a phenomenon related to CCP5 enzyme activity.

As microtubules in multicilia are glutamylated, we assessed whether loss of *Agbl5* affected the glutamylation level in ependymal multicilia using immunofluorescence (IF). Ependymal cells differentiate during the first postnatal week (Spassky et al., 2005). At P7, the GT335-positive multicilia appear as short tufts in the wild-type LV (Figure 5C-F), with only a few in the dorsal wall, but more in the lateral and middle walls (Figure 5C-F, K). In the *Agbl5*$^{M1/M1}$ mice, the number of GT335-positive multicilia tufts were comparable with that of wild-type mice in all three walls (Figure 5K), but the intensity (Figure 5C-F vs. 5G-J) and the length of GT335 signal in the multicilia (Figure 5L) were both strongly increased. Therefore, loss of *Agbl5* indeed increased the glutamylation level in ependymal multicilia.

To determine whether loss of *Agbl5* affects other types of tubulin PTM in ependymal multicilia, the expression of tubulin acetylation, another conserved PTM of ciliary axoneme was assessed. Interestingly, compared with that in wild-type mice (Figure 5M-P), the intensity and length of acetylated tubulin signal in the multicilia of mutant mice were dramatically reduced (Figure 5R-U). Therefore, loss of *Agbl5* increased the level of tubulin glutamylation at the expense of acetylation level in multicilia, reflecting a balance between two types of modifications. When measured with the signal of Arl13b, a protein localized on ciliary membrane (Caspary et al., 2007), the length of multicilia was not significantly

different between wild-type and mutant mice (Figure 5N-T, V), indicating that loss of *Agbl5* did not alter the length of ependymal cilia at this stage.

Ependymal cilia in *Agbl5*$^{M1/M1}$ are initially motile

Given the unchanged number of ependymal multicilia in *Agbl5*$^{M1/M1}$ mice at early stages, we assessed their function by imaging their beating pattern in P15 mice using a high-speed camera. At this stage ependymal multicilia of *Agbl5*$^{M1/M1}$ mice were formed in a density similar to those in wild-type (Figure 6A, B) and were motile (Figure 6C, Movie 5). Those bundled multicilia beat at frequencies comparable with that of wild-type mice (Figure 6D). However, in contrast to wild-type ependyma where multicilia of neighboring cells largely beat in the same direction (Figure 6A, C, E, Movie 4), those in mutant mice often beat in different directions (Figure 6B, C, E, Movie 5). In certain individual ependymal cells of the mutant mouse, cilia in the same cell can beat in different directions (Figure 6C, closed arrowheads; Movie 5, arrows). Therefore, the multicilia in *Agbl5*$^{M1/M1}$ ependymal cells are initially formed, but their intercellular beating coordination are impaired.

The displacement of BB patches in *Agbl5*$^{M1/M1}$ ependymal cells is impaired

In P45 *Agbl5*$^{M1/M1}$ mice, BBs are dispersed over the surface of ependymal cells (Figure 3O, P, R). It is possible that the aberrant BB positioning at this late stage is secondary to the loss of multicilia, because ependymal ciliary beating induces the formation of actin networks that stabilize BBs (Mahuzier et al., 2018). To this end, we assessed the BB displacement in ependymal cells of mice at P15, when the ependymal multicilia are still present in the mutant. The whole-mount of the lateral walls of LVs were co-immunostained with Centrin and β-catenin to label the BBs and cell boundary respectively (Figure 6F, G). The displacement of BB patches is measured as the distance between the center of BB patch and that of the apical cell surface normalized to the distance between the cell surface center and boundary in the

same direction (Figure 6J, (Ohata et al., 2014; Mirzadeh et al., 2010)). We found that the displacement of BB patches in *Agbl5*$^{M1/M1}$ ependymal cells is significantly reduced compared with that in wild-type (K).

In differentiated ependymal cells, BB patches tend to align in similar directions among the neighboring cells, reflecting a tissue-level polarity (Mirzadeh et al., 2010; Hirota et al., 2010; Ohata et al., 2014; Takagishi et al., 2017). We measured the BB angles by drawing vectors from the center of cell apical surface to the center of the BB patch in each cell (Figure 6H, I). The distribution of BB patch angles is significantly more diverse in the mutant than that in the wild-type ependyma (Figure 6L). These results suggest that *Agbl5* contributes to BB positioning at early stage.

Loss of the enzyme activity of CCP5 alone is not sufficient to cause hydrocephalus

In order to confirm that the loss of ependymal cilia in *Agbl5*^{M1} mutants did not solely result from the inactivity of CCP5 enzyme, we generated a second *Agbl5* mutant allele (designated *Agbl5*^{M2}) where a region spanning exon 6 and intron 8 that encodes a part of CP domain of CCP5, was replaced with IRES-guided tdTomato reporter (Figure 7A). This mutant mimics the one we reported previously (Wu et al., 2017). The absence of *Agbl5* transcripts was confirmed in the testis, brain, and eye of *Agbl5*$^{M2/M2}$ mice (Figure 7B).

Traced with the tdTomato reporter, the expression of *Agbl5* was also detected in the ependymal cell layer of the lateral ventricles in *Agbl5*^{M2} heterozygous mice at P7 (Figure 7C, D), similar to our observations in the *Agbl5*^{M1} allele (Figure 4B, Figure S3C). Consistent with the previously reported *Agbl5* KO mice (Wu et al., 2017; Giordano et al., 2019), *Agbl5*$^{M2/M2}$ do not exhibit obvious anomaly other than male infertility. No enlarged cerebral ventricles were observed even in 3-month old mice (Figure 7E, F).

We wondered whether mutations in two *Agbl5* mutants alter the glutamylation level to different degrees. Immunoblotting assessment revealed that compared with the wild-type, the GT335 immunoreactivity was increased in *Agbl5*$^{M2/M2}$ brain to an extent similar to that in *Agbl5*$^{M1/M1}$ mice (Figure 7G). Immunofluorescence assay further revealed that similar to that in the *Agbl5*^{M1} mutant, the intensity of GT335 signal in ependymal multicilia was also increased, accompanied by the reduction in the

immunosignals of acetylated tubulin (Figure 7H-O). These results emphasized that loss of CCP5 enzyme activity contributes to the altered PTM levels in ependymal multicilia of both *Agbl5* mutants, which though is not necessary to be deleterious.

Therefore, the elevated glutamylation level in *Agbl5* mutants are attributed to the loss of CCP5 enzyme activity, which alone is not sufficient to induce hydrocephalus.

Discussion

Polyglutamylation is a conserved PTM on cilia axonemal microtubules. In contrary to its writers that have been linked to ciliary architecture and motility, the role of polyglutamylation erasers in cilia has not been fully appreciated. This is largely due to the absence of a broad spectrum of ciliopathic phenotypes (other than photoreceptor degeneration and male infertility) in their mammalian mutants. In this study, using a null *Agbl5* allele (*Agbl5*^{M1}), we demonstrated that *Agbl5* is essential for the development of ependymal cells in cerebral ventricle to maintain the brain homeostasis. Particularly, deletion of the N-terminal domain of CCP5 along with partial CP domain impairs the stability of multicilia in ependymal cells, leading to lethal hydrocephalus. In this mutant, ependymal multicilia are initially formed but the synchronousness of their beating is compromised. Moreover, the BB patches in individual cells are not properly positioned and the compact apical actin networks around basal bodies are disrupted. In contrast, the mutation solely targeting the CP domain of CCP5 did not cause enlarged ventricles, despite the altered PTM status in ependymal cilia. This study uncovers a novel role of *Agbl5* and emphasizes the requirement of its N-domain in ependymal multicilia development.

The development of ependymal cell is involved in the establishment of polarity on three levels, i.e. rotational polarity (the unidirectional orientation of basal feet in the same cluster of multicilia), translational polarity (the polarized positioning of the BB patch at one side of the cell surface), and tissue polarity (the synchronized multicilia beating direction/rhythm across the tissue) (Mirzadeh et al., 2010; Mahuzier et al., 2018; Boutin et al., 2014; Arata et al., 2022). In *Agbl5*$^{M1/M1}$ mice, the multicilia are initially formed, but their intercellular beating coordination is compromised, suggesting an aberrant tissue polarity. In addition, the displacement of BB patches in individual ependymal cells is also impaired,

indicating a defect in translational polarity. Therefore, CCP5 apparently contributes to the establishment of both translational and tissue polarities in ependymal cells.

It is unexpected that loss of CCP5, a MT modification enzyme exhibits profound effects on actin-related functions in ependymal cells, at least in two aspects. Firstly, loss of CCP5 in *Agbl5*$^{M1/M1}$ impairs the displacement of BB patches in ependymal cells. The establishment of translational polarity in ependymal cells relies on the actomyosin dynamics (Hirota et al., 2010). Particularly, the phosphorylation of non-muscle myosin 2 (NMII) is essential for the polarized localization of BB patches (Hirota et al., 2010). It will be intriguing to further determine how the expression and/or localization of phosphorylated NMII are altered in *Agbl5*$^{M1/M1}$ ependymal cells. Secondly, the apical actin networks in the mutant ependymal cells are severely disrupted in *Agbl5*$^{M1/M1}$ ependymal cells, while the BBs in ependymal cells are not properly aligned, suggesting a possible defect in the sub-apical actin networks around BBs as well (Werner et al., 2011; Mahuzier et al., 2018; Arata et al., 2022). It remains unknown how CCP5 is involved in assembly of actin networks in ependymal cells. A recent study demonstrated that the regulators of tubulin polyglutamylase complex are involved in MT association of actin nucleators and MT–actin crosslinkers, exemplified the role of polyglutamylation enzymes in bridging functions between these two types of cytoskeleton (Wang et al., 2022). Given the important role of apical actin networks in maintaining the stability of BBs (Mahuzier et al., 2018), its aberrance likely contributes to the loss of multicilia in *Agbl5*$^{M1/M1}$ ependymal cells in response to the sheering of CSF. Moreover, the impaired local synchronization of cilia can cause the steric collision (Ringers et al., 2023), which may generate additional force to stub the cilia rooted in a uncompact actin network.

Planar cell polarity (PCP) pathway is essential for the establishment of rotational and tissue polarities in ependymal cells, but only fine-tunes the translation polarity (Ohata et al., 2014; Boutin et al., 2014). It requires further determination whether CCP5, particularly its N-domain is involved in the expression/localization of PCP core proteins in ependymal cells. In fully mature ependymal cells, two sets of MTs exist. In addition to one set that goes along with the actin meshwork and underlines the patch of BBs, another set is polarized and extended between the patch and the cell cortex, providing an anchoring

point at the cell cortex in the similar location in neighboring cells (Boutin et al., 2014). The latter serves as a component of tissue polarity that is required for asymmetric PCP protein localization in each cell (Boutin et al., 2014; Vladar et al., 2012). Recently, the structure of CCP5 in complex with MTs revealed that the N-domain of CCP5 forms a β sandwich structure and coordinates with its CP domain to recognize the C-terminal tail of tubulins (Chen et al., 2024). The N-domain exposed on the outer surface of MT may render additional interface to direct the polarization of MTs that provide the arching point to the cortex and thereby regulate the localization of PCP core proteins in ependymal cells. It is also tempting to conceive that CCP5 may regulate PCP components directly. A recent study revealed that Disheveleds (Dvls), the cytosol adaptors of PCP pathway are polyglutamylated at their C-termini, which regulates the distribution of these molecules in the condensates (Kravec et al., 2024). However, CCP5 does not degrade the α-linked polyglutamate at the C-termini of Dvls despite their colocalization.

In monociliated cells, we showed that CCP5 interacts with the ciliation negative regulator CP110 through its N-domain (Wang et al., 2023). Although loss of CP110 also caused asynchronous ciliary beating, reduced motility and randomization of directionality, or a complete loss of motility in multicilia cells (Walentek et al.), similar to what were seen in *Agbl5*$^{M1/M1}$ ependymal cells, we did not detect significant reduction of CP110 expression *in Agbl5*$^{M1/M1}$ lateral ventricles (data not shown). Different from primary cilia, CP110 localizes to the motile cilia-forming basal bodies. In multiciliated cells, it is specially needed for ciliary adhesion complex formation (Antoniades et al., 2014) and basal body interactions with the actin cytoskeleton (Walentek et al.). It requires further investigation how CCP5 and CP110 coordinate in multicilia development or whether CCP5 requires additional mediators to facilitate the unique polarized placement of multicilia in ependymal cells.

Using two *Agbl5* mutant models, this study revealed the role of CCP5 beyond its enzyme activity. It was surprising that although loss of CCP5 enzyme activity results in elevated glutamylation level in ependymal cilia, it is not necessary to be deleterious. In the *Agbl5*$^{M1/M1}$ mutant, the majority of initially formed ependymal cilia beat with a normal frequency, suggesting a functional compensation for the

increased glutamylation level in the multicilia axoneme. Prominently, loss of CCP5 increased glutamylation level at the expense of tubulin acetylation in ependymal cilia. Similar observation was reported in the connecting cilia of retina in an *Agbl5* mutant mouse (Aljammal et al., 2024). Although these two modifications take place at different locations in the MT, both are characteristic of stable MTs. Therefore, a complementary/compensation mechanism that regulates the balance between these two modifications in axoneme apparently exists.

Supported by *in vivo* evidence, the present study reinforces the speculation that the unique N-domain in CCP family may have a role specifically related to cilium/centrioles (Wang et al., 2023; Rodriguez de la Vega Otazo et al., 2013). In *Agbl5*$^{M2/M2}$ mice, the transcripts coding CCP5 N-terminus are still present (data not shown), making it possible that this region still fulfills the function to regulate or recruit other proteins and thereby mitigates the deleterious effects (Wu et al., 2017; Giordano et al., 2019). Such candidates may include other CCP members (e.g. CCP6) that degrade long chain polyglutamate of non-tubulin substrates important for cilium/centrioles function (Hao et al., 2021; Kravec et al., 2024). Given the unique possession of the N-domain in CCP family, generation of the mutant alleles of other CCP members with deleted N-domain can further provide insights in this regard.

Taken together, this study uncovered an unappreciated function of *Agbl5* in ependymal cell development, and provides a novel clue contributing to the positioning, coordination, and maintenance of ependymal multicilia mediated by a polyglutamylation enzyme though beyond its role to modify the ciliary axoneme.

Materials and Methods

Animals

Mice colonies were maintained in a SPF animal facility on a 12-hr light: 12-hr dark cycle with free access to food and water. All animal study protocols were approved by the Institutional Animal Care and Use Committee (IACUC) at Tianjin University.

Generation of novel *Agbl5* mutant alleles

Two *Agbl5* mutant alleles (*Agbl5*^{M1} and *Agbl5*^{M2}) were created using CRISPR-CAS9 gene editing system on C57BL/6N background by Biocytogen Co., Beijing, China. To generate *Agbl5*^{M1} allele, sgRNA 5'-AGCAGCAGACCCACTAGCGG-3' and 5'-TCTCAGCTCTATGGAAGACG-3', which target the sequence next to the start codon and intron 8 respectively, together with the donor plasmid harboring tdTomato reporter cassette flanked with 3'- and 5'- homologous arms, and Cas9 mRNA were injected into zygotes with well-recognized pronuclei. To generate *Agbl5*^{M2} allele, sgRNA 5'-AACATGAAAGCCGTATTCTTGGG-3' and 5'-TCTATGGAAGACGGGGGTGCTGG-3', which target exon 6 and intron 8 respectively, together with the donor plasmid harboring an IRES guided tdTomato reporter cassette flanked with 3'- and 5'- homologous arms, and Cas9 mRNA were injected into zygotes with well-recognized pronuclei. The founders (F0) were determined by genotyping PCR. After bred with wild-type mice, the F1 mice with desired mutation were selected after genotyping, and the integration and copy number of the inserted fragment were further validated with Southern blotting. *Agbl5* mutant heterozygous mice were inbred to produce homozygous and wild-type litter mates. The *Agbl5* mutant and wild-type alleles were genotyped using primers listed in Table S3.

Off-target determination

The online CRISPR-CAS9 target prediction tool CCTOP (Stemmer et al., 2015) or COSMID (Cradick et al., 2014) were used to predict off-targets of the sgRNAs used in generation of *Agbl5* mutant alleles. Eleven top-ranking predicted off-targets for each sgRNA were selected and primers to amplify the

predicted genomic region were designed using primer3 software. With the genome DNA from heterozygous offspring of 2 independent founders as the template, the amplicons of predicted off-targets were obtained using *pfu* polymerase enzyme and subsequently subjected to Sanger sequencing after gel extraction. Sequences of amplified predicted off-target regions of wild-type and mutants were aligned to the sequences from UCSC genome browser using CLCBIO main workbench software. The absence of predicted off-targets was confirmed in both *Agbl5* mutant alleles. The assessed list of predicted off-targets were provided in Tables S1 and S2, and the sequencing results are available upon request.

RT-PCR analysis of *Agbl5* expression

Total RNA was extracted from testis, brain, eye, and spleen of P45 *Agbl5* mutant mice or wild-type litter mates using Trizol reagent (CWBIO, Taizhou, China) according to manufacturer's protocol. First strand cDNA was synthesized using ABScript first strand cDNA synthesis kit (ABclonal, Wuhan, China) according to manufacturer's instructions. Expression of *Agbl5* was analyzed by subsequent PCR using primers 5'-TCTCTGGATGGACTTCGTGT-3' and 5'-TGGTTCGTGGGACTCTTGG-3'. *β-actin* amplified using primers 5'- ATATCGCTGCGCTGGTCGTC-3' and 5'-AGGATGGCGTGAGGGAGAGC-3' was used as a control.

Detection of tdTomato fluorescence

Mice were subjected to transcardiac perfusion with PBS followed by 2% paraformaldehyde (PFA) after anesthesia with 10% chloral hydrate. Brains were dissected and fixed with 2% PFA overnight at 4°C. Brains were embedded in Tissue-Tek OCT (Sakura, China) after cryoprotection in 30% sucrose and sectioned in 20 μm thick coronally. After wash with PBS, brain sections were subjected to confocal images directly.

Analysis of the flow of CSF using Evans Blue

The circulation of CSF was analyzed by using Evans Blue dye as previously described (Liu et al., 2016). Mice of age P30 were anesthetized with Avertin. The 30-gauge needle attached to syringe was positioned at specific bregma points of 0.1 mm posterior and 1.0 mm on the head. Five microliters of Evans blue dye (diluted as 4% in PBS) were carefully and gradually injected into the right lateral ventricle (LV) of each mouse. 20 min later, mice were sacrificed and whole brains were dissected and fixed in 4% PFA for 12 hr. The samples were then embedded in agarose (4% in PBS) and kept at 4°C for 30 mints to solidify. Coronal sections were cut to inspect the presence of dye in each part of the ventricular system. Images were captured by using a stereomicroscope (SMZ1270, Nikon, Japan) equipped with a digital camera (Nikon, Japan).

Immunofluorescence and Histological analysis

Mice were subjected to transcardiac perfusion with PBS followed by 4% paraformaldehyde (PFA) after anesthesia with 10% chloral hydrate. Brains were dissected and fixed with 4% PFA overnight at 4°C. Tissues were embedded in paraffin after dehydration with graded concentrations of ethanol and xylene or in OCT after cryoprotection with 30% sucrose in PBS. Paraffin-embedded brains were sectioned coronally in 8 μm or 12 μm thick using a microtome (MICROM HM 325, Thermo Scientific, China). Hematoxylin-eosin staining was done according to standard protocols and then slides were mounted with a mounting medium (Wuxi Jiangyuan, Wuxi, China). Images of brain sections were taken using a stereomicroscope (Nikon, Japan) equipped a camera (ToupTek, China) to obtain the whole view of desired ventricular compartments or using Nikon eclipse Ci (Nikon, Japan) equipped with a Micropublisher 6 camera (Teledyne Photometric, Tucson, USA) for imaging lateral ventricles only.

The immunofluorescence on brain sections was done according to standard protocols. Sections were incubated with primary antibodies GT335 (AG-20B-0020, Adipogen, USA, 1:500), mouse anti-acetylated-tubulin (T6793, Sigma, USA, 1:500), mouse anti-Foxj1(eBioscience, France, clone 2A5,

1:200), rabbit anti-Arl13b (17711–1-AP, Proteintech, China, 1:500), rabbit anti-RFP (ab62341, Abcam, USA, 1:500), rabbit anti-vimentin (10366-1-AP, Proteintech, China, 1:200), rabbit anti-Tdtomato (600-401, Rockland, USA, 1:200), rabbit anti-s100b (EP1576Y, Abcam, USA, 1:200) at 4°C overnight and then the immunosignals were visualized by incubation with secondary antibodies Alexa Fluor® 594 donkey anti-rabbit IgG (1:750) and/or Alexa Fluor® 488 goat anti-mouse IgG (1:750) for 1 h at room temperature. Sections were dipped in PBS containing DAPI for 5 min followed by 3 washes with PBS before mounted with antifade mounting reagent (Fluoromount-G (0100-35, SounthernBiotech, USA). To quantify the number of cells positive for specific markers, 3 serious slides with at least 3 sections on each slide were manually counted under immunofluorescence microscope.

Fluorescence microscopy imaging

All the samples were observed at room temperature under a fluorescence microscope (ECLIPSE 80i; Nikon, Tokyo, Japan) equipped with a 40 × 0.75 NA objective lens (Nikon) or a confocal microscope (TCS SP8; Leica, Wetzlar, Germany) equipped with 63 ×1.4 NA objective lens (Leica). Images were acquired using NIS-Elements software (Nikon) or Las X software (Leica). Image processing was performed using ImageJ and Photoshop (Adobe, California, USA).

Quantification of the length of multicilia

The length of multicilia was manually measured on images of brain sections stained with Ar13b, GT335, and anti-acetylated tubulin antibody. Stained sections were imaged under a confocal microscope (TCS SP8; Leica) equipped with 63 × 1.4 NA objective lens (Leica) and manually measured on Image J software using segmented line tool to quantify the longest cilia of each multicilia bundle.

Scanning electron microscopy

Mouse LV walls were dissected and fixed overnight at 4°C in 2.5% glutaraldehyde in PBS. After post-fixed in 1% osmium tetroxide, the samples were dehydrated through a series of graded ethanol (30%,

50%, 75%, 95%, and 100%) and critical-point dried using CO_2 as the transitional fluid. Samples were mounted and sputter coated with gold, and images were captured with a Leo 1530 FEG scanning electron microscope (Zeiss, Germany) at an accelerating voltage of 5 KV.

Immunoblotting

Mouse tissues were homogenized in the RIPA buffer containing the cOmplete® EDTA-free protease inhibitors (Roche Diagnostics, Mannheim, Germany). After centrifuge at 12,000 rpm for 10 min at 4°C, proteins in the supernatant were separated with 10% SDS-PAGE and then transferred to nitrocellulose membranes. Membranes were blocked with 5% no-fat milk for 30 min, followed by incubation with antibody GT335 (Adipogen, USA, 1:5000) or EP1332Y (Abcam, USA, 1:6000) overnight at 4°C. After washing with 0.1% TBST for 3 times, membranes were incubated with the HRP-conjugated goat anti-mouse or donkey anti-rabbit secondary antibodies (Bioss, Beijing, China) for 2 hr at room temperature. After 3 times wash with 0.1% TBST, the immunoreactivities of proteins were visualized with Western bright ECL reagent (Advansta, Menlo Park, USA).

Preparation of whole-mounts lateral ventricles

Whole-mounts of the lateral ventricles were prepared as described (Ohata et al., 2014; Pan et al., 2023). Briefly, mice were euthanized with CO_2, and the lateral ventricles were carefully dissected at a thickness of 500-1,000 μm using Vannas Scissors (66VT, 54140B) in pre-warmed (37°C) dissection solution (25 mM Hepes,117.2 mM NaCl, 26.1 mM $NaHCO_3$, 5.3 mM KCl, 1.8 mM $CaCl_2$, 0.81 mM $MgSO_4$, 1 mM $NaH_2PO_4 \cdot 2H_2O$, and 5.6 mM Glucose, pH 7.4).

High-speed imaging of ciliary beating and whole-mount immunostaining

Live imaging of ciliary beating and immunostaining were performed as described (Ohata et al., 2014; Pan et al., 2023; Zhao et al., 2021) with minor modifications. For high-speed imaging of ciliary

beating, the whole-mount preparations were incubated with SiR-tubulin (100 nM; Spirochrome, SC002) in DMEM (Thermo Fisher, 12430062) supplemented with 0.3 mg/ml glutamine, 100 U/ml penicillin, and 100 U/ml streptomycin for 1 h at 37℃ to label the cilia. Ciliary beating was captured with 5 ms exposure time at 100 frames per second (fps) at 37℃ using an Olympus Xplore SpinSR 10 microscope equipped with UPLAPO OHR 60 × /1.50 Objective Lens, Hamamatsu ORCA-Fusion camera, 4,000 rpm CSU Disk Speed, and OBIS Laser.

For immunostaining, freshly dissected whole-mounts of the lateral ventricles were pre-permeabilized with 0.5% Triton X-100 in PBS for 30 sec before fixation to remove soluble proteins and fixed for 15 min in 4% paraformaldehyde. After fixation, the whole-mounts were extracted with 0.5% Triton X-100 in PBS for 15 min and blocked in 4% BSA/TBST blocking solution at room temperature (RT) for 1 h. Next, they were incubated with primary antibodies overnight at 4°C. After three washes with the blocking solution for 5 min each, the whole-mounts were incubated with secondary antibodies at RT for 1h, and mounted with ProLongTM (Thermo Fisher, 2273640). Primary antibodies include mouse IgG anti-acetylated-tubulin (1:1,000; Sigma-Aldrich, T6793), rabbit anti-Centrin 1 (1:200, Proteintech, 12794-1-AP), rabbit anti-β-catenin (1:200, Proteintech, 51067-2-AP), rabbit IgG anti-Cep164 (1:200; Proteintech Group Inc, 22227-1-AP). Secondary antibodies are Alexa Fluor 647 goat anti-mouse IgG (1:1,000; Life Technologies, A-21236), Alexa Fluor 488 donkey anti-rabbit IgG (1:1,000; Life Technologies, A-21206), and Alexa Fluor 568 goat anti-rabbit IgG (1:750; Invitrogen, A-11011). Actin is stained with Phalloidin-TRITC (1:1,000; Sigma, P1951). The confocal images were acquired using Leica SP8 or the Olympus Xplore SpinSR 10 microscope. Three-dimensional structured illumination microscopy (3D-SIM) super-resolution images were acquired using the DeltaVision OMX SR imaging system (GE Healthcare). The z-axis scanning step was 0.125 μm and raw images were processed in SoftWoRx 7.0 software by the following procedures: OMX SI Reconstruction, OMX Image Registration, and maximum intensity projection.

Quantification of cilia beating direction and frequency

The beating direction and frequency were measured using the software FIJI (NIH, USA). For the frequency analysis, the Kymography tool was applied. The R package ggplot2 rendered the analysis of beating directions.

Quantification of BB patch displacement and angle distribution

The BB patch displacement was measured as the ratio of the distance between the center of BB patch and the cell centroid to the distance between the cell centroid and cell boundary in the same direction as described (Mirzadeh et al., 2010; Ohata et al., 2014). These distances and cell centroids are determined using Fiji software. The statistics was analyzed using Student's *t* test.

To determine the BB patch angle distribution in a given field, vectors were drawn from the cell centroids to the centers of BB patches. The angles of the vectors were measured in Fiji software. Deviations of individual cell's BB patch angle from the median within the field were calculated and plotted as a histogram using a program that we generated using MATLAB. The percentages were calculated with a bin size of 10°. Ependymal cells within 5 different fields (120 μm x 120 μm for each field) were analyzed. The statistics for the BB angle distribution was analyzed using Watson's two-sample U^2 test according to(Zar, 1999) in MATLAB.

Statistical Analysis

Data are presented as the mean ± SEM and the statistics was analyzed using Student's *t* test unless otherwise specified. Kaplan-Meier Curves between the wild-type and *Agbl5*$^{M1/M1}$ mice was proceeded with a log rank (Mantel-Cox) test. All statistical analysis was performed with GraphPad Prism, $p<0.05$ were considered statistically significant.

Data Availability Statement

The lists of assessed predicted off-targets for the mutant mice were provided in Table S1 and S2. Other original data and program codes are available upon request.

Acknowledgements

We thank Dr. Corey Powell from Consulting for Statistics, Computing, and Analytics Research (CSCAR), University of Michigan for assistance with ciliary beating direction analysis, Dr. Eric Rentchler from the Microscopy Core of Biomedical Research Core Facilities, University of Michigan Medical School for advances on ciliary beating frequency analysis. This work is partially supported by the start-up to HYW from Tianjin University and Elizabeth E. Kennedy Children's Research Award to HYW from the Department of Pediatrics, University of Michigan Medical School.

References

Aljammal, R., T. Saravanan, T. Guan, S. Rhodes, M.A. Robichaux, and V. Ramamurthy. 2024. Excessive tubulin glutamylation leads to progressive cone-rod dystrophy and loss of outer segment integrity. *Human Molecular Genetics*. 33:802–817. doi:10.1093/hmg/ddae013.

Antoniades, I., P. Stylianou, and P.A. Skourides. 2014. Making the connection: ciliary adhesion complexes anchor basal bodies to the actin cytoskeleton. *Developmental Cell*. 28:70–80. doi:10.1016/j.devcel.2013.12.003.

Arata, M., F.M. Usami, and T. Fujimori. 2022. Coordination of Cilia Movements in Multi-Ciliated Cells. *J Dev Biol*. 10:47. doi:10.3390/jdb10040047.

Boutin, C., P. Labedan, J. Dimidschstein, F. Richard, H. Cremer, P. André, Y. Yang, M. Montcouquiol, A.M. Goffinet, and F. Tissir. 2014. A dual role for planar cell polarity genes in ciliated cells. *Proc. Natl. Acad. Sci. U.S.A.* 111:E3129–38. doi:10.1073/pnas.1404988111.

Caspary, T., C.E. Larkins, and K.V. Anderson. 2007. The graded response to Sonic Hedgehog depends on cilia architecture. *Developmental Cell*. 12:767–778. doi:10.1016/j.devcel.2007.03.004.

Chen, J., E.A. Zehr, J.M. Gruschus, A. Szyk, Y. Liu, M.E. Tanner, N. Tjandra, and A. Roll-Mecak. 2024. Tubulin code eraser CCP5 binds branch glutamates by substrate deformation. *Nature*. 631:905–912. doi:10.1038/s41586-024-07699-0.

Cradick, T.J., P. Qiu, C.M. Lee, E.J. Fine, and G. Bao. 2014. COSMID: A Web-based Tool for Identifying and Validating CRISPR/Cas Off-target Sites. *Mol Ther Nucleic Acids*. 3:e214. doi:10.1038/mtna.2014.64.

Delgehyr, N., A. Meunier, M. Faucourt, M. Bosch Grau, L. Strehl, C. Janke, and N. Spassky. 2015. Ependymal cell differentiation, from monociliated to multiciliated cells. *Methods Cell Biol*. 127:19–35. doi:10.1016/bs.mcb.2015.01.004.

Giordano, T., S. Gadadhar, S. Bodakuntla, J. Straub, S. Leboucher, G. Martinez, W. Chemlali, C. Bosc, A. Andrieux, I. Bièche, C. Arnoult, S. Geimer, and C. Janke. 2019. Loss of the deglutamylase CCP5 perturbs multiple steps of spermatogenesis and leads to male infertility. *Journal of Cell Science*. 132. doi:10.1242/jcs.226951.

Graser, S., Y.-D. Stierhof, S.B. Lavoie, O.S. Gassner, S. Lamla, M. Le Clech, and E.A. Nigg. 2007. Cep164, a novel centriole appendage protein required for primary cilium formation. *J Cell Biol*. 179:321–330. doi:10.1083/jcb.200707181.

Hao, K., Y. Chen, X. Yan, and X. Zhu. 2021. Cilia locally synthesize proteins to sustain their ultrastructure and functions. *Nature Communications*. 12:6971. doi:10.1038/s41467-021-27298-1.

Haycraft, C.J., Q. Zhang, B. Song, W.S. Jackson, P.J. Detloff, R. Serra, and B.K. Yoder. 2007. Intraflagellar transport is essential for endochondral bone formation. *Development*. 134:307–316. doi:10.1242/dev.02732.

He, K., X. Ma, T. Xu, Y. Li, A. Hodge, Q. Zhang, J. Torline, Y. Huang, J. Zhao, K. Ling, and J. Hu. 2018. Axoneme polyglutamylation regulated by Joubert syndrome protein ARL13B controls ciliary targeting of signaling molecules. *Nature Communications*. 1–14. doi:10.1038/s41467-018-05867-1.

Hirota, Y., A. Meunier, S. Huang, T. Shimozawa, O. Yamada, Y.S. Kida, M. Inoue, T. Ito, H. Kato, M. Sakaguchi, T. Sunabori, M.-A. Nakaya, S. Nonaka, T. Ogura, H. Higuchi, H. Okano, N. Spassky, and K. Sawamoto. 2010. Planar polarity of multiciliated ependymal cells involves the anterior migration of basal bodies regulated by non-muscle myosin II. *Development*. 137:3037–3046. doi:10.1242/dev.050120.

Ikegami, K., S. Sato, K. Nakamura, L.E. Ostrowski, and M. Setou. 2010. Tubulin polyglutamylation is essential for airway ciliary function through the regulation of beating asymmetry. *Proc. Natl. Acad. Sci. U.S.A.* 107:10490–10495. doi:10.1073/pnas.1002128107.

Jacquet, B.V., R. Salinas-Mondragon, H. Liang, B. Therit, J.D. Buie, M. Dykstra, K. Campbell, L.E. Ostrowski, S.L. Brody, and H.T. Ghashghaei. 2009. FoxJ1-dependent gene expression is required for differentiation of radial glia into ependymal cells and a subset of astrocytes in the postnatal brain. *Development*. 136:4021–4031. doi:10.1242/dev.041129.

Janke, C., K. Rogowski, D. Wloga, C. Regnard, A.V. Kajava, J.-M. Strub, N. Temurak, J. van Dijk, D. Boucher, A. Van Dorsselaer, S. Suryavanshi, J. Gaertig, and B. Eddé. 2005. Tubulin polyglutamylase enzymes are members of the TTL domain protein family. *Science*. 308:1758–1762. doi:10.1126/science.1113010.

Kahle, K.T., A.V. Kulkarni, D.D. Limbrick, and B.C. Warf. 2016. Hydrocephalus in children. *Lancet*. 387:788–799. doi:10.1016/S0140-6736(15)60694-8.

Kalinina, E., R. Biswas, I. Berezniuk, A. Hermoso, F.X. Aviles, and L.D. Fricker. 2007. A novel subfamily of mouse cytosolic carboxypeptidases. *The FASEB Journal*. 21:836–850. doi:10.1096/fj.06-7329com.

Kimura, Y., N. Kurabe, K. Ikegami, K. Tsutsumi, Y. Konishi, O.I. Kaplan, H. Kunitomo, Y. Iino, O.E. Blacque, and M. Setou. 2010. Identification of tubulin deglutamylase among Caenorhabditis elegans and mammalian cytosolic carboxypeptidases (CCPs). *J. Biol. Chem.* 285:22936–22941. doi:10.1074/jbc.C110.128280.

Kravec, M., O. Šedo, J. Nedvědová, M. Micka, M. Šulcová, N. Zezula, K. Gömöryová, D. Potěšil, R. Sri Ganji, S. Bologna, I. Červenka, Z. Zdráhal, J. Harnoš, K. Tripsianes, C. Janke, C. Barinka, and V. Bryja. 2024. Carboxy-terminal polyglutamylation regulates signaling and phase separation of the Dishevelled protein. *The EMBO Journal*. doi:10.1038/s44318-024-00254-7.

Kundishora, A.J., A.K. Singh, G. Allington, P.Q. Duy, J. Ryou, S.L. Alper, S.C. Jin, and K.T. Kahle. 2021. Genomics of human congenital hydrocephalus. *Childs Nerv Syst*. 1–16. doi:10.1007/s00381-021-05230-8.

Kyrousi, C., Z. Lygerou, and S. Taraviras. 2017. How a radial glial cell decides to become a multiciliated ependymal cell. *Glia*. 65:1032–1042. doi:10.1002/glia.23118.

Lacroix, B., J. van Dijk, N.D. Gold, J. Guizetti, G. Aldrian-Herrada, K. Rogowski, D.W. Gerlich, and C. Janke. 2010. Tubulin polyglutamylation stimulates spastin-mediated microtubule severing. *J Cell Biol*. 189:945–954. doi:10.1083/jcb.201001024.

Lechtreck, K.-F., P. Delmotte, M.L. Robinson, M.J. Sanderson, and G.B. Witman. 2008. Mutations in Hydin impair ciliary motility in mice. *J Cell Biol*. 180:633–643. doi:10.1083/jcb.200710162.

Liu, M., Z. Guan, Q. Shen, P. Lalor, U. Fitzgerald, T. O'Brien, P. Dockery, and S. Shen. 2016. Ulk4 Is Essential for Ciliogenesis and CSF Flow. *J Neurosci*. 36:7589–7600. doi:10.1523/JNEUROSCI.0621-16.2016.

Lyons, P.J., M.R. Sapio, and L.D. Fricker. 2013. Zebrafish Cytosolic Carboxypeptidases 1 and 5 Are Essential for Embryonic Development. *Journal of Biological Chemistry*. 288:30454–30462. doi:10.1074/jbc.M113.497933.

Lyu, Q., Q. Li, J. Zhou, and H. Zhao. 2024. Formation and function of multiciliated cells. *J Cell Biol*. 223. doi:10.1083/jcb.202307150.

Mahuzier, A., A. Shihavuddin, C. Fournier, P. Lansade, M. Faucourt, N. Menezes, A. Meunier, M. Garfa-Traoré, M.-F. Carlier, R. Voituriez, A. Genovesio, N. Spassky, and N. Delgehyr. 2018. Ependymal cilia beating induces an actin network to protect centrioles against shear stress. *Nature Communications*. 9:2279–15. doi:10.1038/s41467-018-04676-w.

Marques, M.M., J. Villoch-Fernandez, L. Maeso-Alonso, S. Fuertes-Alvarez, and M.C. Marin. 2019. The Trp73 Mutant Mice: A Ciliopathy Model That Uncouples Ciliogenesis From Planar Cell Polarity. *Front Genet*. 10:154. doi:10.3389/fgene.2019.00154.

Marszalek, J.R., P. Ruiz-Lozano, E. Roberts, K.R. Chien, and L.S. Goldstein. 1999. Situs inversus and embryonic ciliary morphogenesis defects in mouse mutants lacking the KIF3A subunit of kinesin-II. *Proceedings of the National Academy of Sciences*. 96:5043–5048. doi:10.1073/pnas.96.9.5043.

Mirzadeh, Z., Y.-G. Han, M. Soriano-Navarro, J.M. García-Verdugo, and A. Alvarez-Buylla. 2010. Cilia organize ependymal planar polarity. *J Neurosci*. 30:2600–2610. doi:10.1523/JNEUROSCI.3744-09.2010.

Ohata, S., and A. Alvarez-Buylla. 2016. Planar Organization of Multiciliated Ependymal (E1) Cells in the Brain Ventricular Epithelium. *Trends in Neurosciences*. 39:543–551. doi:10.1016/j.tins.2016.05.004.

Ohata, S., J. Nakatani, V. Herranz-Pérez, J. Cheng, H. Belinson, T. Inubushi, W.D. Snider, J.M. García-Verdugo, A. Wynshaw-Boris, and A. Alvarez-Buylla. 2014. Loss of Dishevelleds disrupts planar polarity in ependymal motile cilia and results in hydrocephalus. *Neuron*. 83:558–571. doi:10.1016/j.neuron.2014.06.022.

Pan, X., C. Fang, C. Shen, X. Li, L. Xie, L. Li, S. Huang, X. Yan, and X. Zhu. 2023. Basal body contains a “latchbolt” to enable directional ciliary beat across epithelia. *Research Square*. doi:10.21203/rs.3.rs-3499253/v1.

Rimsa, V., T.C. Eadsforth, R.P. Joosten, and W.N. Hunter. 2014. High-resolution structure of the M14-type cytosolic carboxypeptidase from Burkholderia cenocepacia refined exploiting PDB_REDO strategies. *Acta Crystallogr. D Biol. Crystallogr.* 70:279–289. doi:10.1107/S1399004713026801.

Ringers, C., S. Bialonski, M. Ege, A. Solovev, J.N. Hansen, I. Jeong, B.M. Friedrich, and N. Jurisch-Yaksi. 2023. Novel analytical tools reveal that local synchronization of cilia coincides with tissue-scale metachronal waves in zebrafish multiciliated epithelia. *Elife*. 12. doi:10.7554/eLife.77701.

Rodriguez de la Vega Otazo, M., J. Lorenzo, O. Tort, F.X. Aviles, and J.M. Bautista. 2013. Functional segregation and emerging role of cilia-related cytosolic carboxypeptidases (CCPs). *The FASEB Journal*. 27:424–431. doi:10.1096/fj.12-209080.

Rodriguez-Calado, S., P. Van Damme, F.X. Avilés, A.P. Candiota, S. Tanco, and J. Lorenzo. 2023. Proximity Mapping of CCP6 Reveals Its Association with Centrosome Organization and Cilium Assembly. *Int J Mol Sci*. 24:1273. doi:10.3390/ijms24021273.

Rogowski, K., J. van Dijk, M.M. Magiera, C. Bosc, J.-C. Deloulme, A. Bosson, L. Peris, N.D. Gold, B. Lacroix, M. Bosch Grau, N. Bec, C. Larroque, S. Desagher, M. Holzer, A. Andrieux, M.-J. Moutin, and C. Janke. 2010. A family of protein-deglutamylating enzymes associated with neurodegeneration. *Cell*. 143:564–578. doi:10.1016/j.cell.2010.10.014.

Schnitzer, J., W.W. Franke, and M. Schachner. 1981. Immunocytochemical demonstration of vimentin in astrocytes and ependymal cells of developing and adult mouse nervous system. *J Cell Biol*. 90:435–447. doi:10.1083/jcb.90.2.435.

Spassky, N., F.T. Merkle, N. Flames, A.D. Tramontin, J.M. García-Verdugo, and A. Alvarez-Buylla. 2005. Adult ependymal cells are postmitotic and are derived from radial glial cells during embryogenesis. *J Neurosci*. 25:10–18. doi:10.1523/JNEUROSCI.1108-04.2005.

Stemmer, M., T. Thumberger, M. Del Sol Keyer, J. Wittbrodt, and J.L. Mateo. 2015. CCTop: An Intuitive, Flexible and Reliable CRISPR/Cas9 Target Prediction Tool. *PLoS ONE*. 10:e0124633. doi:10.1371/journal.pone.0124633.

Takagishi, M., M. Sawada, S. Ohata, N. Asai, A. Enomoto, K. Takahashi, L. Weng, K. Ushida, H. Ara, S. Matsui, K. Kaibuchi, K. Sawamoto, and M. Takahashi. 2017. Daple Coordinates Planar Polarized Microtubule Dynamics in Ependymal Cells and Contributes to Hydrocephalus. *CellReports*. 20:960–972. doi:10.1016/j.celrep.2017.06.089.

Tort, O., S. Tanco, C. Rocha, I. Bièche, C. Seixas, C. Bosc, A. Andrieux, M.-J. Moutin, F.X. Avilés, J. Lorenzo, and C. Janke. 2014. The cytosolic carboxypeptidases CCP2 and CCP3 catalyze posttranslational removal of acidic amino acids. *Mol. Biol. Cell*. 25:3017–3027. doi:10.1091/mbc.E14-06-1072.

van Dijk, J., K. Rogowski, J. Miro, B. Lacroix, B. Eddé, and C. Janke. 2007. A Targeted Multienzyme Mechanism for Selective Microtubule Polyglutamylation. *Molecular Cell*. 26:437–448. doi:10.1016/j.molcel.2007.04.012.

Viar, G.A., N. Klena, F. Martino, A. Nievergelt, and G. Pigino. 2023. The Tubulin Nano-Code: a protofilament-specific pattern of tubulin post-translational modifications regulates ciliary beating mechanics. *bioRxiv*. 2023.06.28.546853. doi:10.1101/2023.06.28.546853.

Vidovic, D., R.A. Davila, R.M. Gronostajski, T.J. Harvey, and M. Piper. 2018. Transcriptional regulation of ependymal cell maturation within the postnatal brain. *Neural Dev*. 13:2. doi:10.1186/s13064-018-0099-4.

Vladar, E.K., and J.D. Axelrod. 2008. Dishevelled links basal body docking and orientation in ciliated epithelial cells. *Trends in Cell Biology*. 18:517–520. doi:10.1016/j.tcb.2008.08.004.

Vladar, E.K., R.D. Bayly, A.M. Sangoram, M.P. Scott, and J.D. Axelrod. 2012. Microtubules enable the planar cell polarity of airway cilia. *Curr Biol*. 22:2203–2212. doi:10.1016/j.cub.2012.09.046.

Walentek, P., I.K. Quigley, D.I. Sun, U.K. Sajjan, C.K. Elife, 2016. Ciliary transcription factors and miRNAs precisely regulate Cp110 levels required for ciliary adhesions and ciliogenesis. *elifesciences.org*. doi:10.7554/eLife.17557.001.

Wang, L., S.C. Paudyal, Y. Kang, M. Owa, F.-X. Liang, A. Spektor, H. Knaut, I. Sánchez, and B.D. Dynlacht. 2022. Regulators of tubulin polyglutamylation control nuclear shape and cilium disassembly by balancing microtubule and actin assembly. *Cell Res*. 32:190–209. doi:10.1038/s41422-021-00584-9.

Wang, Y., Y. Zhang, X. Guo, Y. Zheng, X. Zhang, S. Feng, and H.-Y. Wu. 2023. CCP5 and CCP6 retain CP110 and negatively regulate ciliogenesis. *BMC Biol*. 21:124–20. doi:10.1186/s12915-023-01622-1.

Werner, M.E., P. Hwang, F. Huisman, P. Taborek, C.C. Yu, and B.J. Mitchell. 2011. Actin and microtubules drive differential aspects of planar cell polarity in multiciliated cells. *J Cell Biol*. 195:19–26. doi:10.1083/jcb.201106110.

Wolff, A., B. de Néchaud, D. Chillet, H. Mazarguil, E. Desbruyères, S. Audebert, B. Edde, F. Gros, and P. Denoulet. 1992. Distribution of glutamylated alpha and beta-tubulin in mouse tissues using a specific monoclonal antibody, GT335. *European Journal of Cell Biology*. 59:425–432.

Wu, H.-Y., P. Wei, and J.I. Morgan. 2017. Role of Cytosolic Carboxypeptidase 5 in Neuronal Survival and Spermatogenesis. *Sci. Rep.* 1–14. doi:10.1038/srep41428.

Xie, H., M. Li, Y. Kang, J. Zhang, and C. Zhao. 2022. Zebrafish: an important model for understanding scoliosis. *Cell. Mol. Life Sci.* 79:506–16. doi:10.1007/s00018-022-04534-5.

Yang, W.-T., S.-R. Hong, K. He, K. Ling, K. Shaiv, J. Hu, and Y.-C. Lin. 2021. The Emerging Roles of Axonemal Glutamylation in Regulation of Cilia Architecture and Functions. *Front Cell Dev Biol*. 9:622302. doi:10.3389/fcell.2021.622302.

Zar, J.H. 1999. Biostatistical Analysis. Prentice Hall, Upper Saddle River, NJ. 1 pp.

Zhang, X., S. Jia, Z. Chen, Y.L. Chong, H. Xie, D. Feng, X. Wu, D.Z. Song, S. Roy, and C. Zhao. 2018. Cilia-driven cerebrospinal fluid flow directs expression of urotensin neuropeptides to straighten the vertebrate body axis. *Nature Publishing Group*. 50:1666–1673. doi:10.1038/s41588-018-0260-3.

Zhao, H., Q. Chen, F. Li, L. Cui, L. Xie, Q. Huang, X. Liang, J. Zhou, X. Yan, and X. Zhu. 2021. Fibrogranular materials function as organizers to ensure the fidelity of multiciliary assembly. *Nature Communications*. 12:1273–15. doi:10.1038/s41467-021-21506-8.

Zou, W., Y. Lv, Z.I. Liu, P. Xia, H. Li, and J. Jiao. 2020. Loss of Rsph9 causes neonatal hydrocephalus with abnormal development of motile cilia in mice. *Sci. Rep.* 10:12435–11. doi:10.1038/s41598-020-69447-4.

Figures

Figure 1

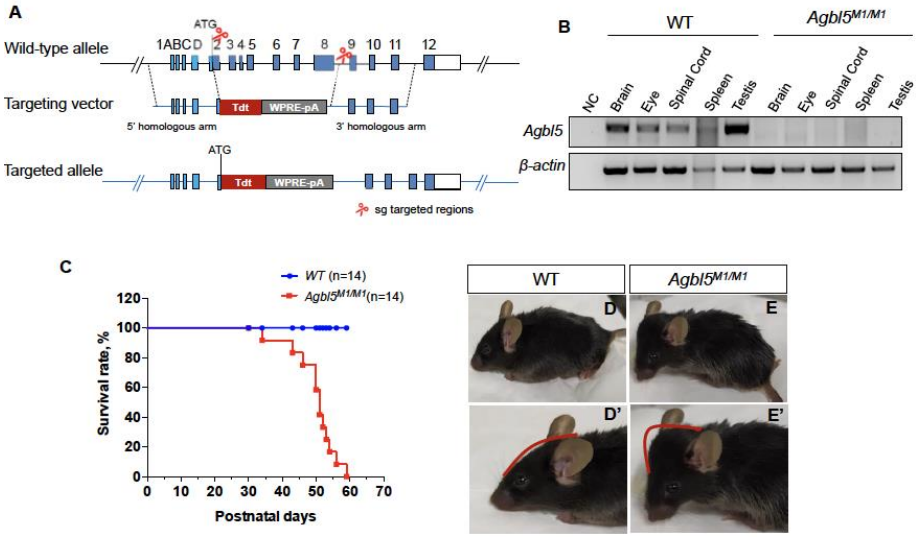

Figure 1. A novel *Agbl5* mutant mouse model exhibited domed head and reduced lifespan. (A) Schematic representation of the knock-out/knock-in strategy to create the novel *Agbl5* mutant (*Agbl5*^{M1}) allele. A region between start codon and intron 8 was replaced with a tdTomato reporter cassette using CRISPR/CAS9 system. (B) RT-PCR using primers targeting a region spanning exon 6 and exon 8 of *Agbl5* confirmed the absence of *Agbl5* transcripts in brain, eye, spinal cord, spleen, and testis of *Agbl5*$^{M1/M1}$ mice. NC, negative control. (C) The Kaplan-Meier survival curve showed that the *Agbl5*$^{M1/M1}$ mice hardly survived more than 50 days (p<0.0005, log-rank (Mantel-Cox) test). (D-E') Representative images of P50 wild-type (D, D') and *Agbl5*$^{M1/M1}$ (E, E') mice. Different from the wild-type mice (D, D'), the mutant (E, E') developed dome-shaped head as indicated with red lines (D', E').

Figure 2

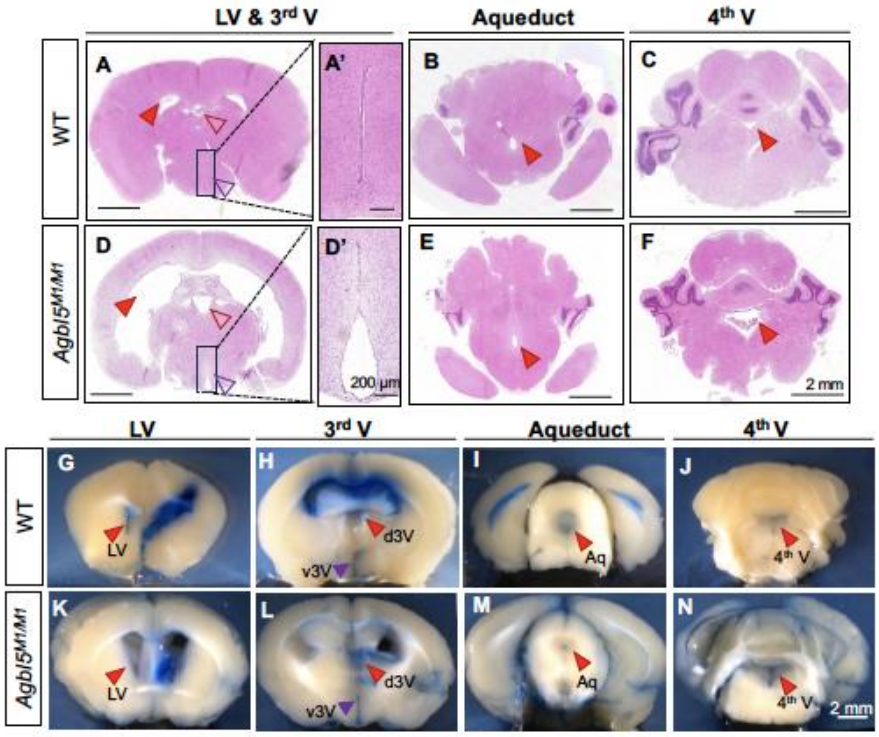

Figure 2. Histological and flow assessment of the cerebrospinal fluid (CSF) pathway. Hematoxylin-Eosin staining on a serial coronal brain sections of P46 wild-type (WT, A-C) and *Agbl5*$^{M1/M1}$ (D-F) mice. Markedly enlarged lateral ventricles (LV, D, closed arrowhead), the third ventricles (D, open arrowheads, D'), and the fourth ventricle (F) were observed in *Agbl5*$^{M1/M1}$ mice compared to the corresponding part in wild-type mice (A, B and C, arrowheads), while the size of the aqueduct was less affected in the mutant (B vs. E, arrowheads). A' and D' are the close view of ventral 3rd ventricles that were indicated in dashed boxes in A and D respectively. The dorsal and ventral 3rd ventricles are pointed with open arrowheads in red and purple respectively in A and D. (G-N) Flow assessment of CSF in mice of P30 intraventricularly injected with Evans Blue. Whole brains were fixed in 4% PFA 20 min later after injection to allow ink distribution and diffusion in the brain of wild-type (G-J) and mutant mice (K-N). Tissue sections showed that diffused ink was clearly observed in the lateral ventricles (LV, red arrowheads in G, K), the third dorsal (d3V, red arrowheads in H, L) and ventral ventricles (v3V, purple arrowheads in H, L), the fourth ventricles (4thV, red arrowheads in J, N) and aqueducts (Aq, red arrowheads in I, M) of both wild-type

(G-J) and mutant (K-N) mice, indicative of communicating hydrocephalus. Scale bars: 2 mm for A-N; 200 μm for A', D'.

Figure 3

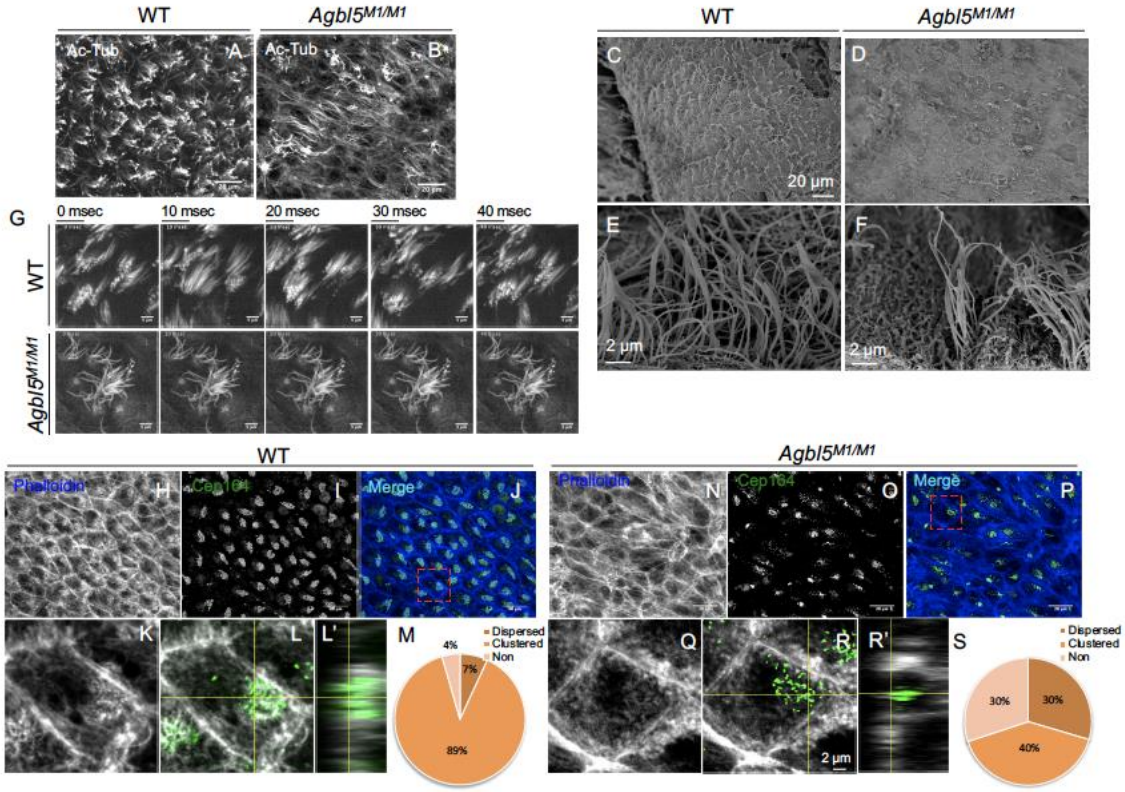

Figure 3. Aberrant ependymal multicilia and basal body positioning in *Agbl5*$^{M1/M1}$ hydrocephalic mice.

(A-B) Representative images of the whole-mount lateral walls of LVs from P45 wild-type (WT, A) or *Agbl5*$^{M1/M1}$ (B) immunostained with the ciliary marker, acetylated tubulin (Act-Tub). While multicilia in WT ependyma evenly cover the ventricle surface and point to the same direction, mutlicilia bundles were scattered with many Act-Tub positive cilia lying on the cell surface. (C-F) Scanning electron microscopy analysis of LV walls from wild-type (C, E) and *Agbl5*$^{M1/M1}$ (D, F) mice of P30. In the wild-type LV, ependymal cells were covered with evenly distributed cilia bundles in a uniformed direction (C), while in the mutant mice, cilia only in the middle of ependymal cell surface remain (D). (E, F) Higher magnification images showed that the length of remaining ependymal cilia in *Agbl5*$^{M1/M1}$ mice (F) is

similar to that in wild-type animal (E). (G) Sequential images of ciliary beating in wild-type (upper row) and *Agbl5*$^{M1/M1}$ (lower row) mice. (H-L, N-R) Whole-mount lateral walls of LVs from P45 wild-type (H-L) or *Agbl5*$^{M1/M1}$ (N-R) immunostained with the centriolar distal appendage marker CEP164 (I, O) with actin network labeled with phalloidin (H, K, N, Q). While BBs are clustered and polarized in the wild-type ependymal cells (I, J), those in the mutant (O, P) are often diffused. The actin networks are largely disrupted in the mutant ependymal cells (N, Q, vs. H, K for wild-type). (K-L', Q-R') Z-projection views of apical actin network around BB in wild-type (K, L) and *Agbl5*$^{M1/M1}$ (Q, R) ependymal cells and respective orthogonal views (L', R'). The mutant ependymal cells lack the compact actin networks even around clustered BBs (R, R'). (M, S) Quantification of ependymal cells with differently distributed BBs in wild-type (M) and *Agbl5*$^{M1/M1}$ mice (S). Scale bar, A-D, H-J, N-P, 20 μm; E-F, K-L', Q-R', 2 μm; G, 5 μm.

Figure 4

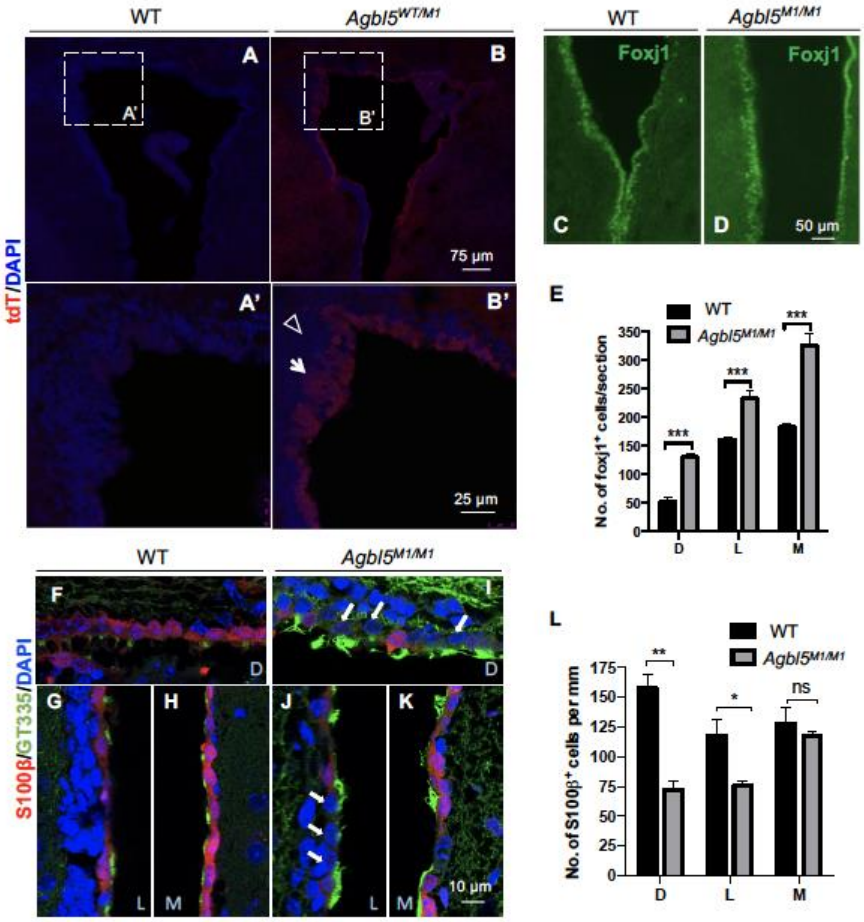

Figure 4. Expression of genes promoting multiciliogenesis is not impaired in *Agbl5*$^{M1/M1}$ ependyma. (A-B') Immunofluorescence analysis revealed that tdTomato signals can be detected in heterozygous *Agbl5*^{M1} (*Agbl5*$^{WT/M1}$) brain (B, B'), but not in the wild-type control (A, A'). The tdTomato signals were localized in the ependymal cells but largely devoid from the subventricular zone (arrowhead). At the dorsal-lateral region of the LV, the tdTomato signals extend to 2-3 layers (arrow). (C, D) Lateral ventricles from P7 wild-type and *Agbl5*$^{M1/M1}$ mice were immunostained with Foxj1, a marker of multiciliation. (E) Quantification showed that the number of Foxj1-positive cells in individual LV walls of the mutant mice (n=5) is increased compared to that in the wild-type mice (n=5). (F-K) Representative images of the dorsal (F, I), lateral (G, J) and middle (H, K) walls of LV from P17 wild-type (F-H) or *Agbl5*$^{M1/M1}$ (I-K) mice that were co-immunostained with S100β (red) and GT335 (green) with nuclei visualized with DAPI (blue). At this age, ependymal cells in all walls of LV are normally S100β-positive

(F-H). In contrast, in *Agbl5*$^{M1/M1}$ mice (I-K) many cells in the ependymal cell layer are not immunoreactive for S100β despite the presence of multicilia (arrows). (L) Quantitative analysis showed that the number of S100β-positive ependymal cells normalized to the length of ventricle walls is significantly reduced in the dorsal and the lateral walls in mutant mice. D, dorsal wall; L, lateral wall; M, middle wall. Error bars represent SEM. *, $p < 0.05$; **, $p<0.01$, ***, $p<0.001$; student's *t*-test. Scale bars, A, B, 75 μm; A', B', 25 μm; C, D, 50 μm; F-K, 10 μm.

Figure 5

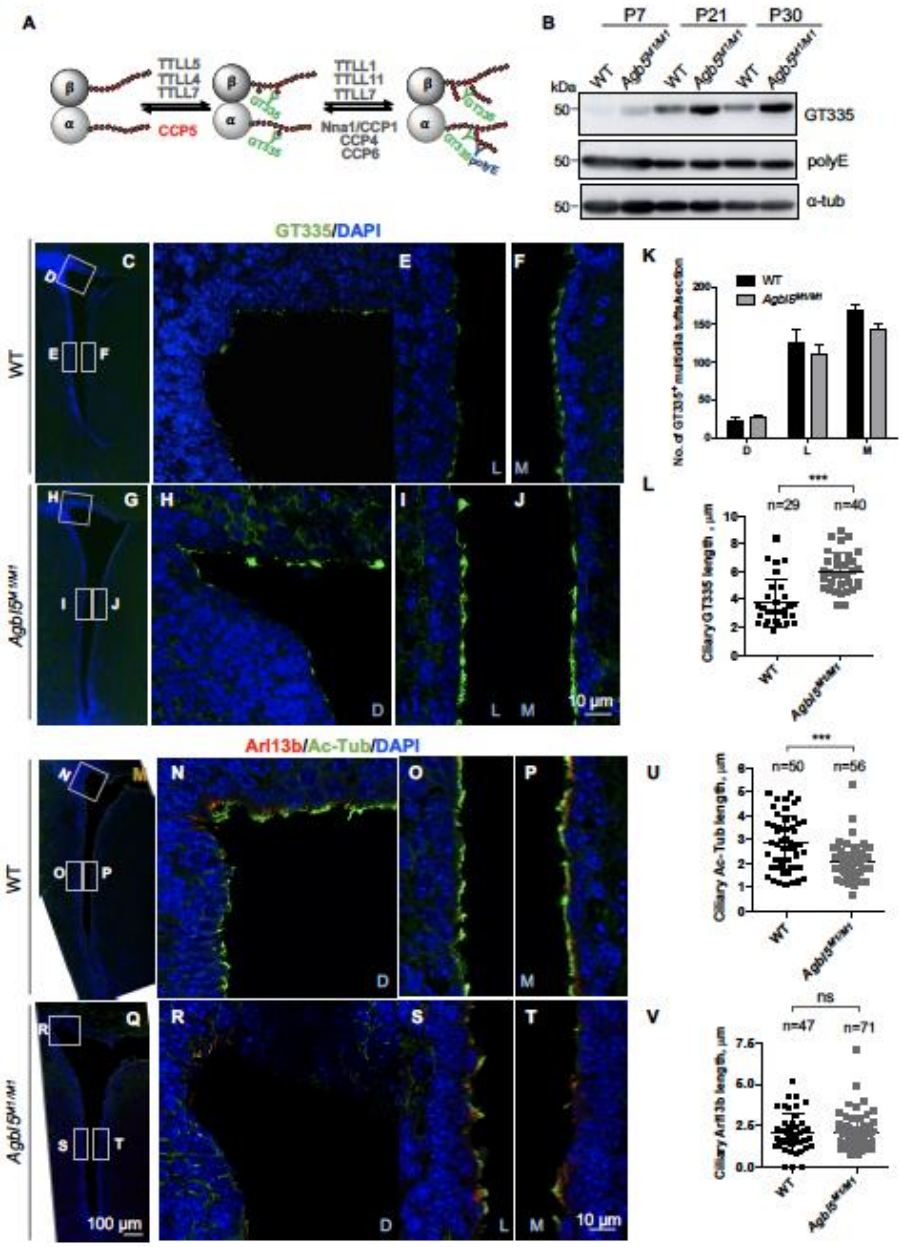

Figure 5. The glutamylation level is increased in ependymal multicilia of *Agbl5*$^{M1/M1}$ mice. (A) A schematic representation shows the enzymes involved in tubulin polyglutamylation and modifications recognized by GT335 and polyE antibodies respectively. (B) Immunoblotting of LV from mice of different ages showed that compared to the wild-type, the immunosignals of GT335 but not that of polyE are increased in *Agbl5*$^{M1/M1}$ mice at all ages examined. (C-J) Lateral ventricles of P7 wild-type (C-F) and

Agbl5$^{M1/M1}$ (G-J) mice stained with GT335 (green) and DAPI. Representative images show that the intensity and length of GT335 immunosignals in ependymal cilia are increased in all three (H, dorsal; I, lateral; J, middle) walls of LV in the mutant mice compared with the respective walls in wild-type LVs (D, dorsal; E, lateral; F, middle). While the number of multicilia tufts are comparable between the wild-type and mutant mice (K), the length of GT335 signals are increased in *Agbl5*$^{M1/M1}$ ependymal cilia (L). (M-T) LVs of wild-type (M-P) and *Agbl5*$^{M1/M1}$ (Q-T) mice co-immunostained with acetylated-tubulin (Ac-Tub, green) and Arl13b (red) with nuclei visualized by DAPI staining. The intensity of acetylated tubulin immunosignals in ependymal cilia are reduced in all three walls of the LV mutant mice (R-T) compared to those of wild-type mice (N-P). The length of ciliary Ac-tub in the lateral wall is also reduced in the mutant (U). (V) Quantification showed that compared to that of the wild-type mice, the length of Arl13b signal in ependymal multicilia of *Agbl5*$^{M1/M1}$ mice were not changed. Letters in blue: D, dorsal wall; L, lateral wall, M, middle wall. Error bars represent SEM, student's *t*-test. Scale bars, C, G, M, Q, 100 μm; D-F, H-J, N-P, R-T, 10 μm.

Figure 6

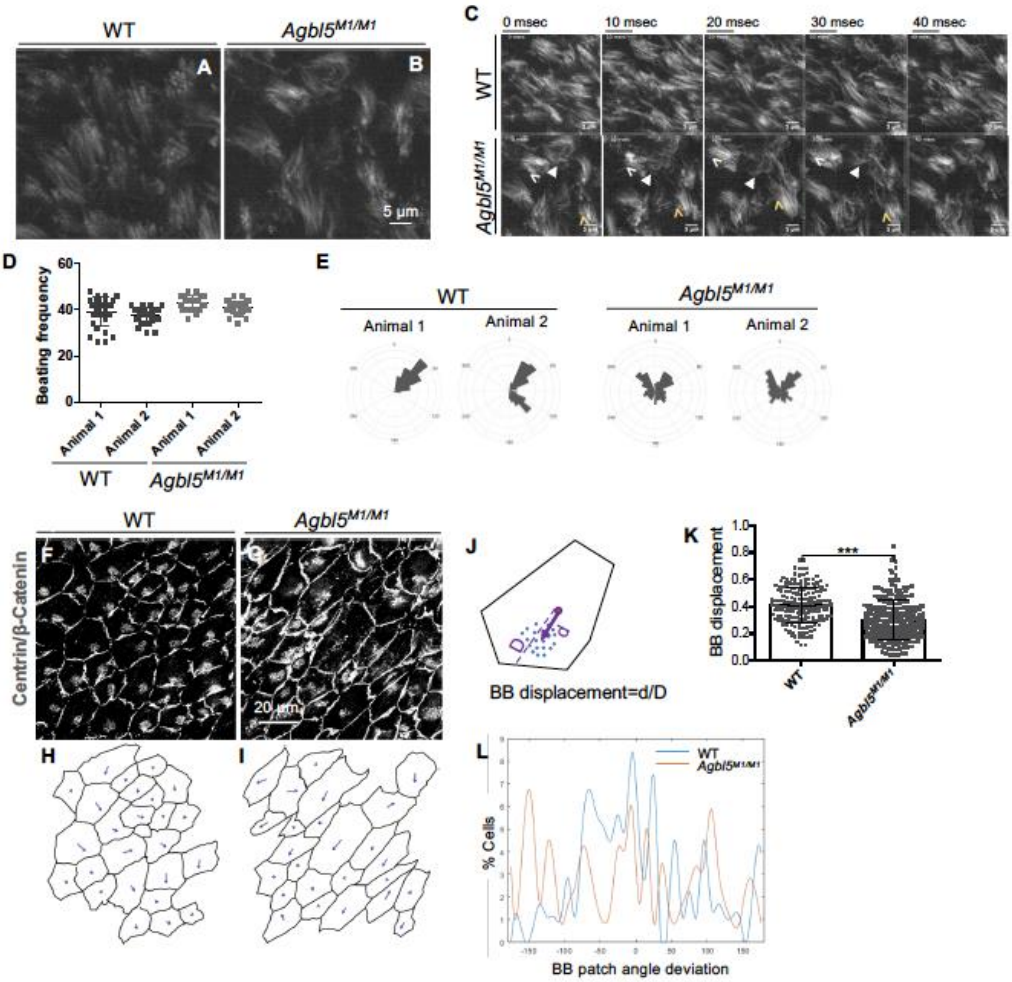

Figure 6. The initially formed ependymal multicilia in *Agbl5*$^{M1/M1}$ mice are motile. (A-B) Images of SiR-tubulin labeled whole-mount LVs from P15 wild-type (A) and *Agbl5*$^{M1/M1}$ (B) mice show that ependymal multicilia are initially formed in the mutant. (C) Sequential images of ciliary beating of P15 wild-type (upper row) and *Agbl5*$^{M1/M1}$ (lower row) showed that the multicilia of wild-type ependymal cells beat in similar direction, while that of mutant are asynchronously. White and yellow open arrowheads indicate respective beating directions of multicilia of two cells; the closed arrowhead points to multicilia of an individual cell beat in opposite directions. (D) Bundled *Agbl5*$^{M1/M1}$ multicilia largely beat at the frequency similar to that of wild-type (n=30 for each animal). Error bars represent SD. (E) Histograms of beating angles for each animal, represented in polar coordinates. The area of each wedge is proportional

to the percentage of angles in the corresponding angle range. (F, G) Whole-mount LVs from P15 wild-type (F) and *Agbl5*$^{M1/M1}$ (G) mice were co-immunostained with Centrin (BB marker) and β-Catenin (cell boundary marker). (H-I) Traces of the intercellular junction labeled with β-Catenin of ependymal cells shown in F and G respectively. The purple arrows show the vectors drawn from the center of the apical surface to that of the BB patch. (J) Diagram showing the measurement of BB patch displacement. (K) Quantification showed that BB patches in *Agbl5*$^{M1/M1}$ ependymal cells are not properly displaced (n= 198 for wild-type; n=253 for the mutant), $p<0.001$, student's *t* test. (L) Histogram of the distribution of BB patch angles in ependymal cells of WT (blue) and *Agbl5*$^{M1/M1}$ (orange), (n=138 for WT; n=119 for the mutant), $p<0.001$, Watson's 2-sample U^2 test. Scale bars, A-C, 5 μm; F, G, 20 μm.

Figure 7

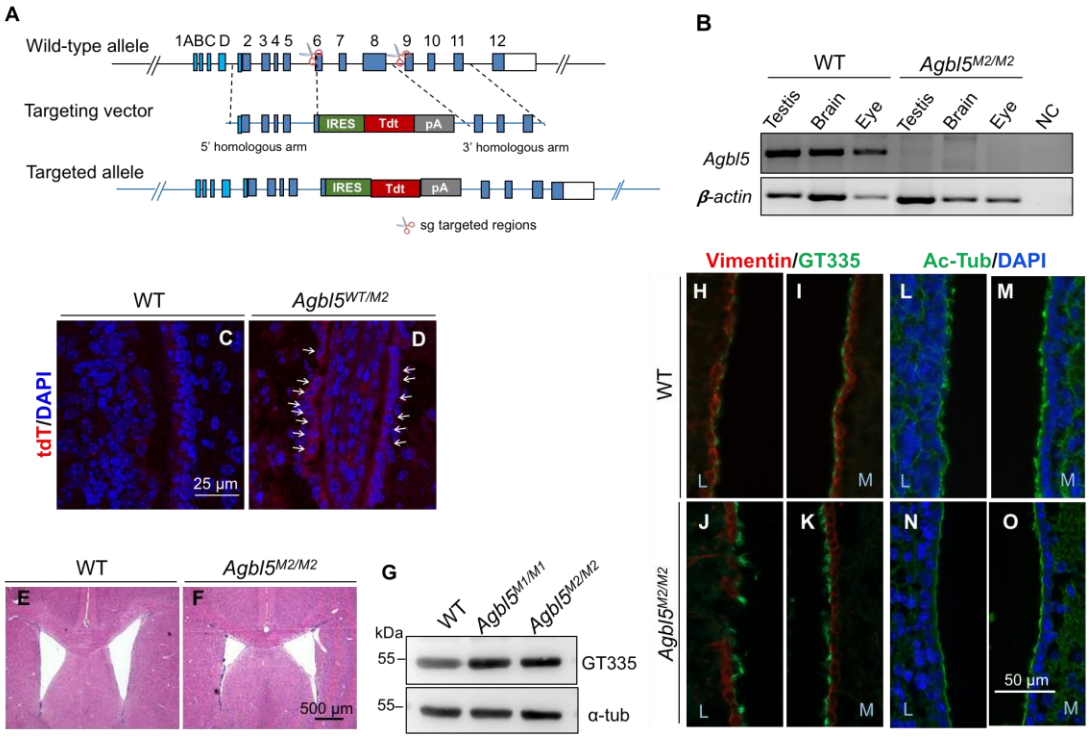

Figure 7. Targeted disruption of CP domain alone in *Agbl5* did not cause hydrocephalus, despite the increased glutamylation in ependymal cilia. (A) Schematic representation of the knock-out/knock-in strategy to create a second *Agbl5* mutant (*Agbl5*^{M2}) allele that resembles the one used in previous

studies (Wu et al., 2017). (B) RT-PCR using primers targeting deleted region in *Agbl5*^{M2} allele confirmed the absence of *Agbl5* transcripts in brain, eye, and testis in *Agbl5*$^{M2/M2}$ mice. NC, negative control. (C-D) Similar to that in *Agbl5*$^{WT/M1}$ mice, tdTomato immunosignal is also detected in ependymal cells of P7 *Agbl*^{M2} heterogenous mice (D, arrows). (E-F) Hematoxylin-Eosin staining of coronal sections of brains from 3-month old wild-type (E) and *Agbl5*$^{M2/M2}$ (F) mice, where no enlarged ventricles were observed. (G) Immunoblotting assay showed that compared with that of wild-type mice, the tubulin glutamylation level was increased in the brain of both *Agbl5* mutants. (H-O) Immunostaining showed that the ciliary GT335 signals in both lateral (J) and middle (K) walls of the LV in *Agbl5*$^{M2/M2}$ mice are increased compared with that in respective walls of the wild-type (H, I). (L-O) The ciliary acetylated-tubulin (Act-Tub) signals are reduced in both lateral (N) and middle (O) walls of the LV in *Agbl5*$^{M2/M2}$ mice compared with respective walls of the wild-type (L, N). L, lateral wall; M, middle wall. Scale bars, C, D, 25 μm; E, F, 500 μm; H-O, 50 μm.

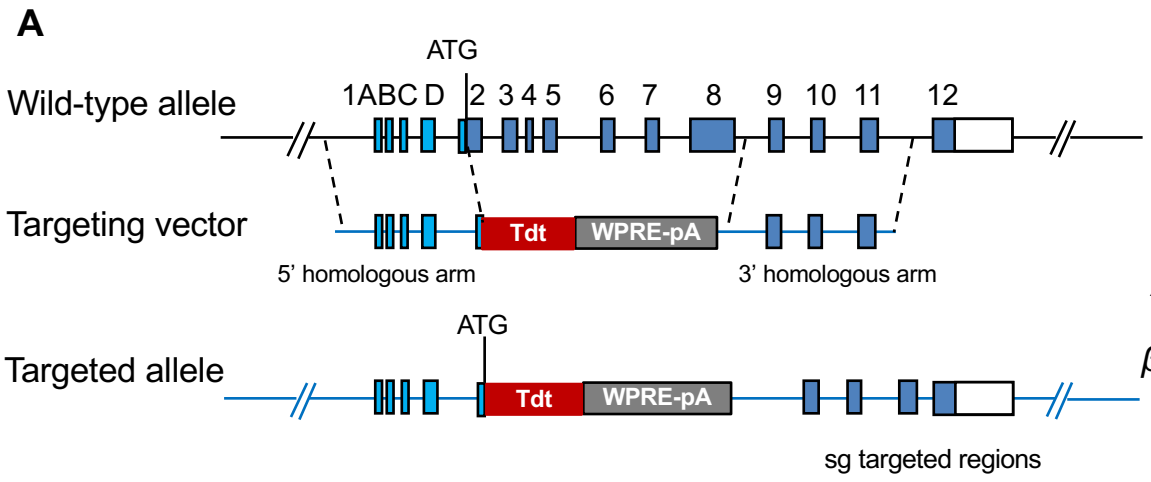
A
ATG
Wild-type allele
1ABC D 2 3 4 5 6 7 8 9 10 11 12
Targeting vector
Tdt
WPRE-pA
5' homologous arm
3' homologous arm
ATG
Targeted allele
Tdt
WPRE-pA
sg targeted regions

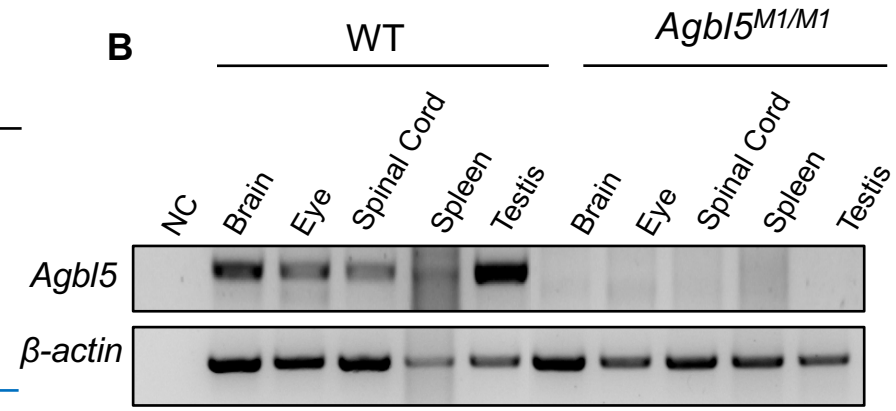
B
WT
Agbl5M1/M1
NC
Brain
Eye
Spinal Cord
Spleen
Testis
Brain
Eye
Spinal Cord
Spleen
Testis
Agbl5
β-actin

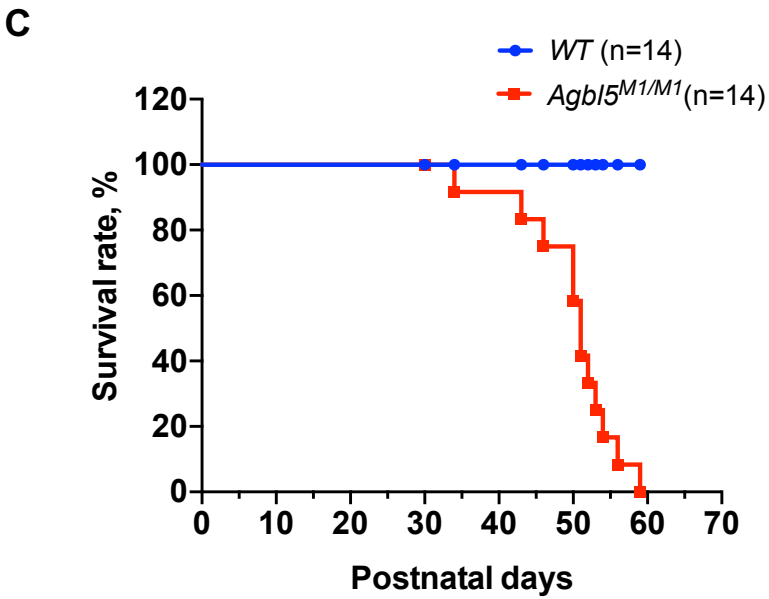
C
WT (n=14)
Agbl5M1/M1(n=14)
Survival rate, %
120
100
80
60
40
20
0
0
10
20
30
40
50
60
70
Postnatal days

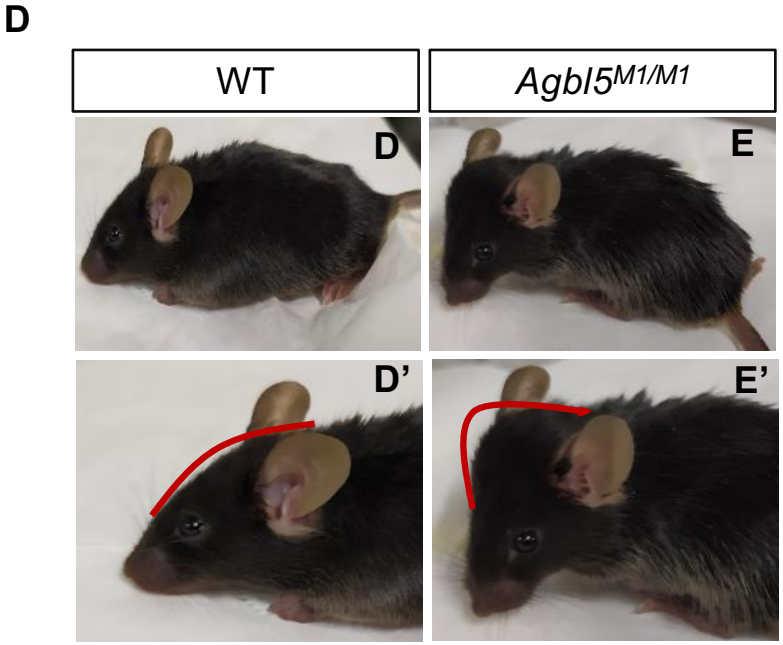
D
WT
Agbl5M1/M1
D
E
D'
E'

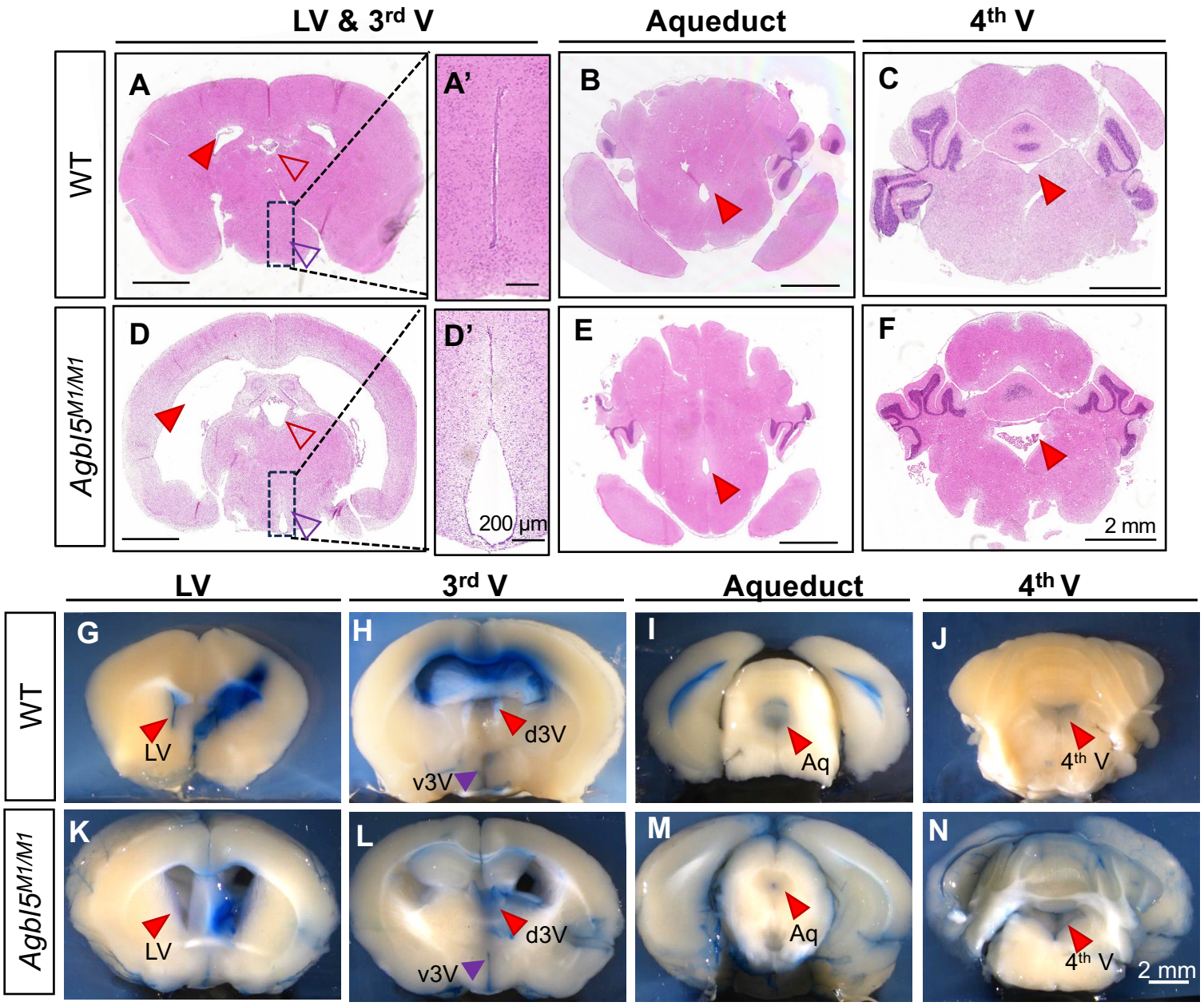
LV & 3rd V
Aqueduct
4th V
WT
AgbI5M1/M1
A
A'
B
C
D
D'
E
F
200 µm
2 mm
LV
3rd V
Aqueduct
4th V
G
H
I
J
K
L
M
N
LV
d3V
v3V
Aq
4th V
2 mm

Figure 2

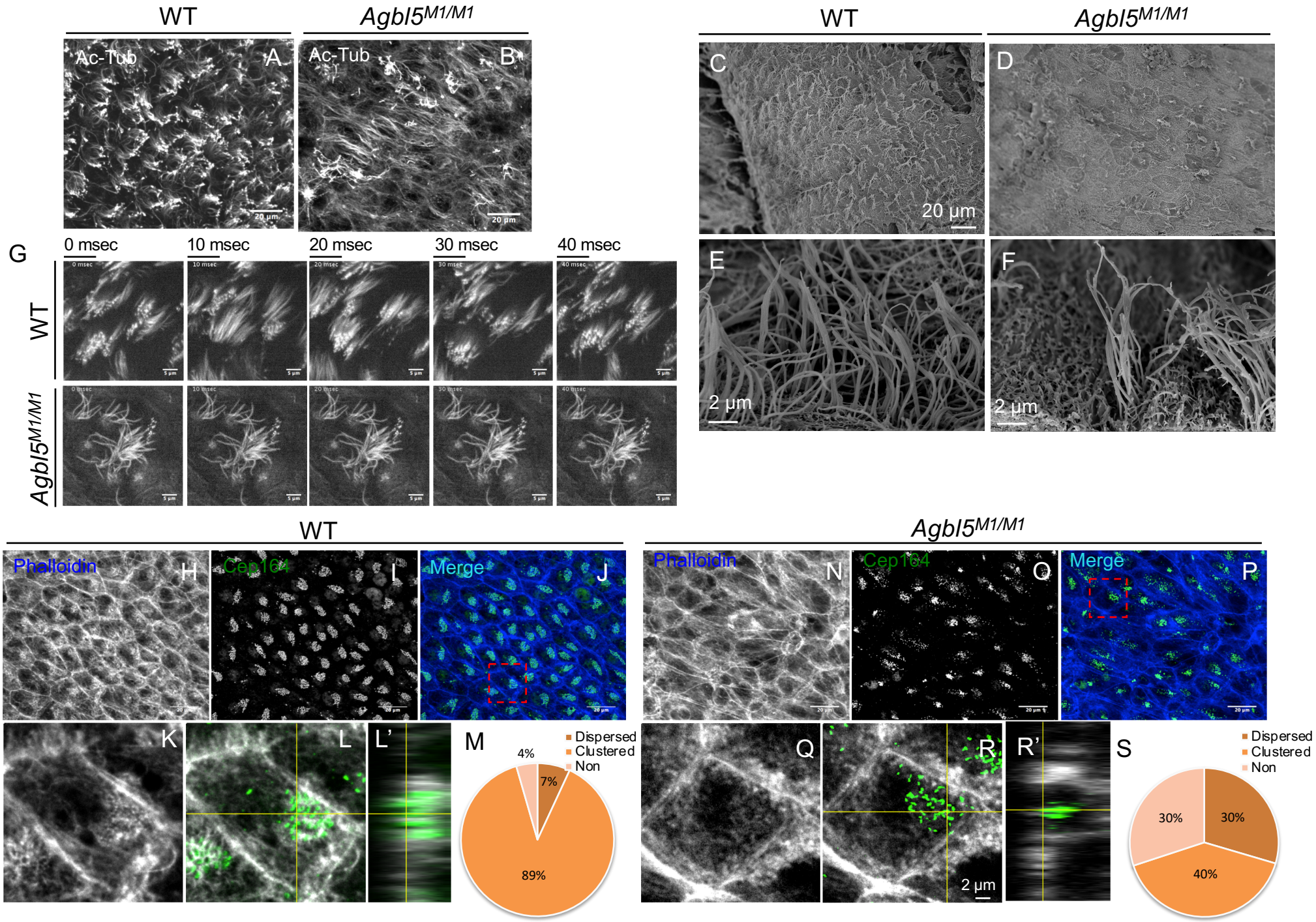
WT
Agbl5M1/M1
Ac-Tub
A
B
20 µm
C
D
E
F
2 µm
G
0 msec
10 msec
20 msec
30 msec
40 msec
WT
Agbl5M1/M1
Phalloidin
Cep164
Merge
H
I
J
K
L
L'
M
Dispersed
Clustered
Non
4%
7%
89%
N
O
P
Q
R
R'
S
30%
30%
40%

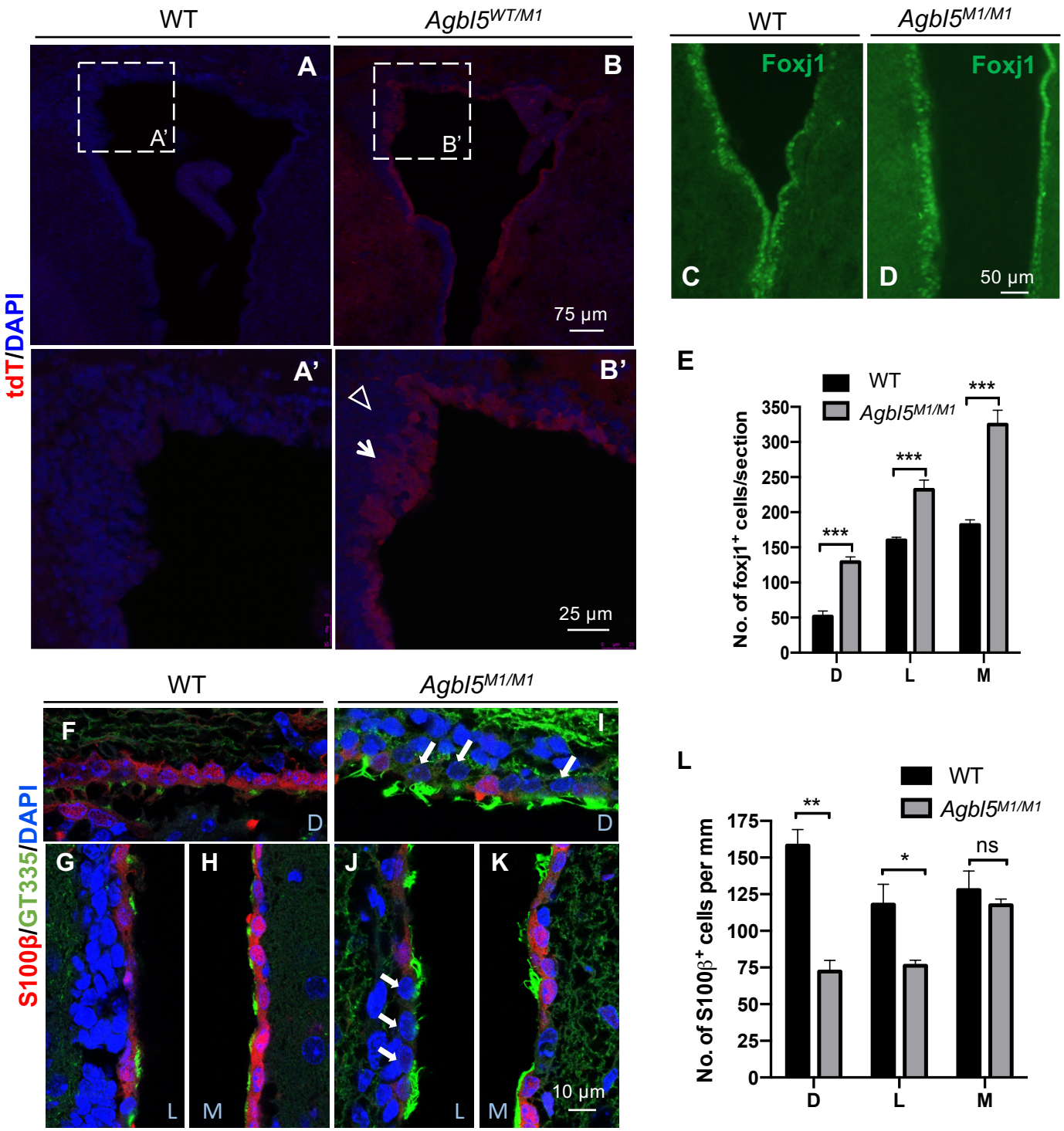
WT
Agbl5WT/M1
tdT/DAPI
A
A'
B
B'
75 µm
25 µm
WT
Agbl5M1/M1
Foxj1
C
D
50 µm
E
WT
Agbl5M1/M1
No. of foxj1+ cells/section
350
300
250
200
150
100
50
0
***
***
***
D
L
M
WT
Agbl5M1/M1
S100β/GT335/DAPI
F
I
D
G
H
J
K
L
M
10 µm
L
WT
Agbl5M1/M1
No. of S100β+ cells per mm
175
150
125
100
75
50
25
0
**
*
ns
D
L
M

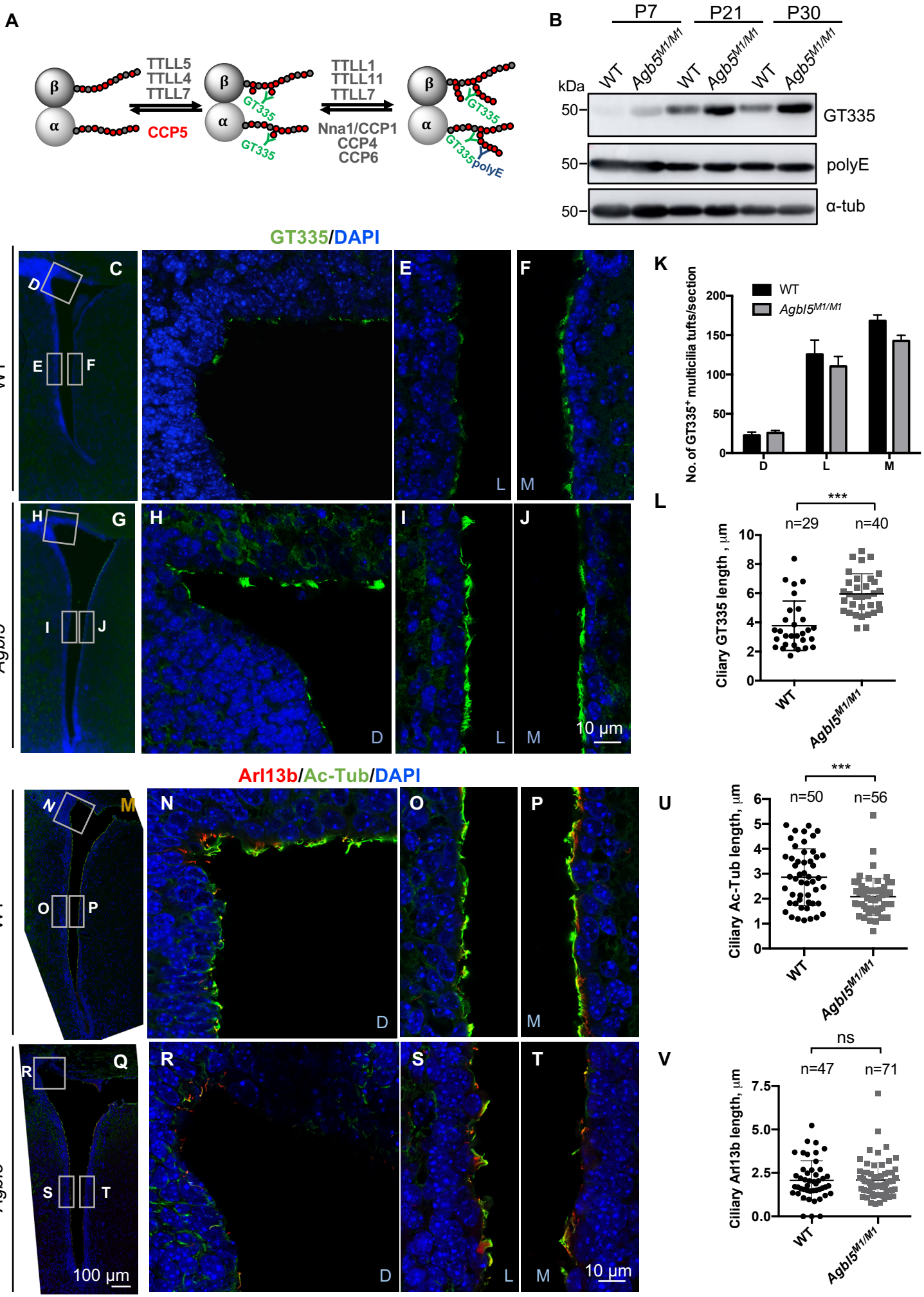
A
β
α
TTLL5
TTLL4
TTLL7
CCP5
GT335
TTLL1
TTLL11
TTLL7
Nna1/CCP1
CCP4
CCP6
polyE
B
P7
P21
P30
WT
Agb5M1/M1
kDa
50
GT335
polyE
α-tub
GT335/DAPI
WT
Agbl5M1/M1
C
D
E
F
G
H
I
J
L
M
10 µm
K
WT
Agbl5M1/M1
No. of GT335+ multicilia tufts/section
200
150
100
50
0
L
***
n=29
n=40
Ciliary GT335 length , µm
10
8
6
4
2
Arl13b/Ac-Tub/DAPI
N
O
P
Q
R
S
T
100 µm
U
n=50
n=56
Ciliary Ac-Tub length, µm
6
5
4
3
2
1
V
ns
n=47
n=71
Ciliary Arl13b length, µm
7.5
5.0
2.5
0.0

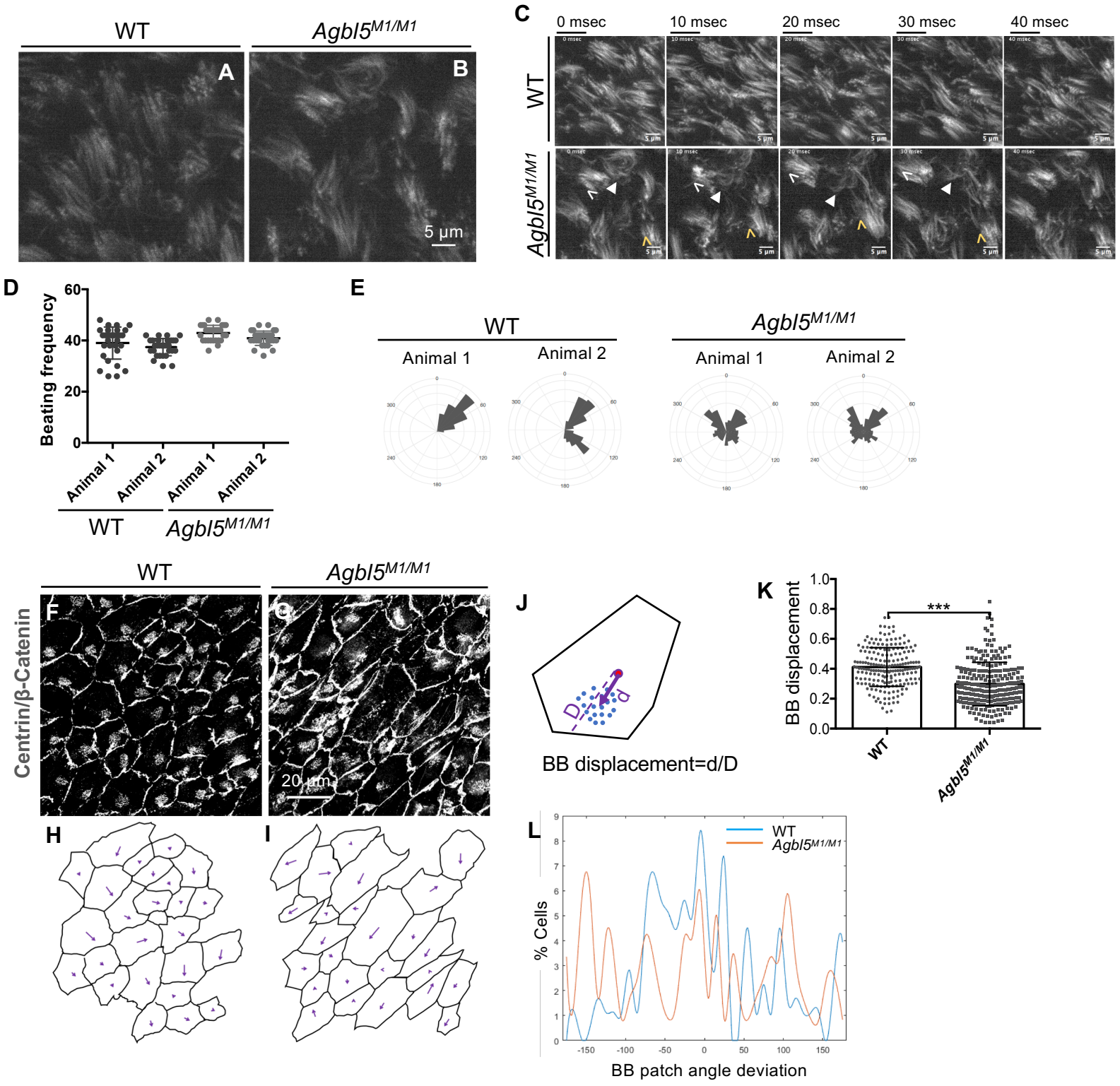
WT
Agbl5M1/M1
A
B
5 µm
C
0 msec
10 msec
20 msec
30 msec
40 msec
WT
Agbl5M1/M1
D
Beating frequency
60
40
20
0
Animal 1
Animal 2
Animal 1
Animal 2
WT
Agbl5M1/M1
E
WT
Agbl5M1/M1
Animal 1
Animal 2
Animal 1
Animal 2
WT
Agbl5M1/M1
Centrin/β-Catenin
F
G
20 µm
H
I
J
D
d
BB displacement=d/D
K
BB displacement
1.0
0.8
0.6
0.4
0.2
0.0
***
WT
Agbl5M1/M1
L
WT
Agbl5M1/M1
% Cells
BB patch angle deviation

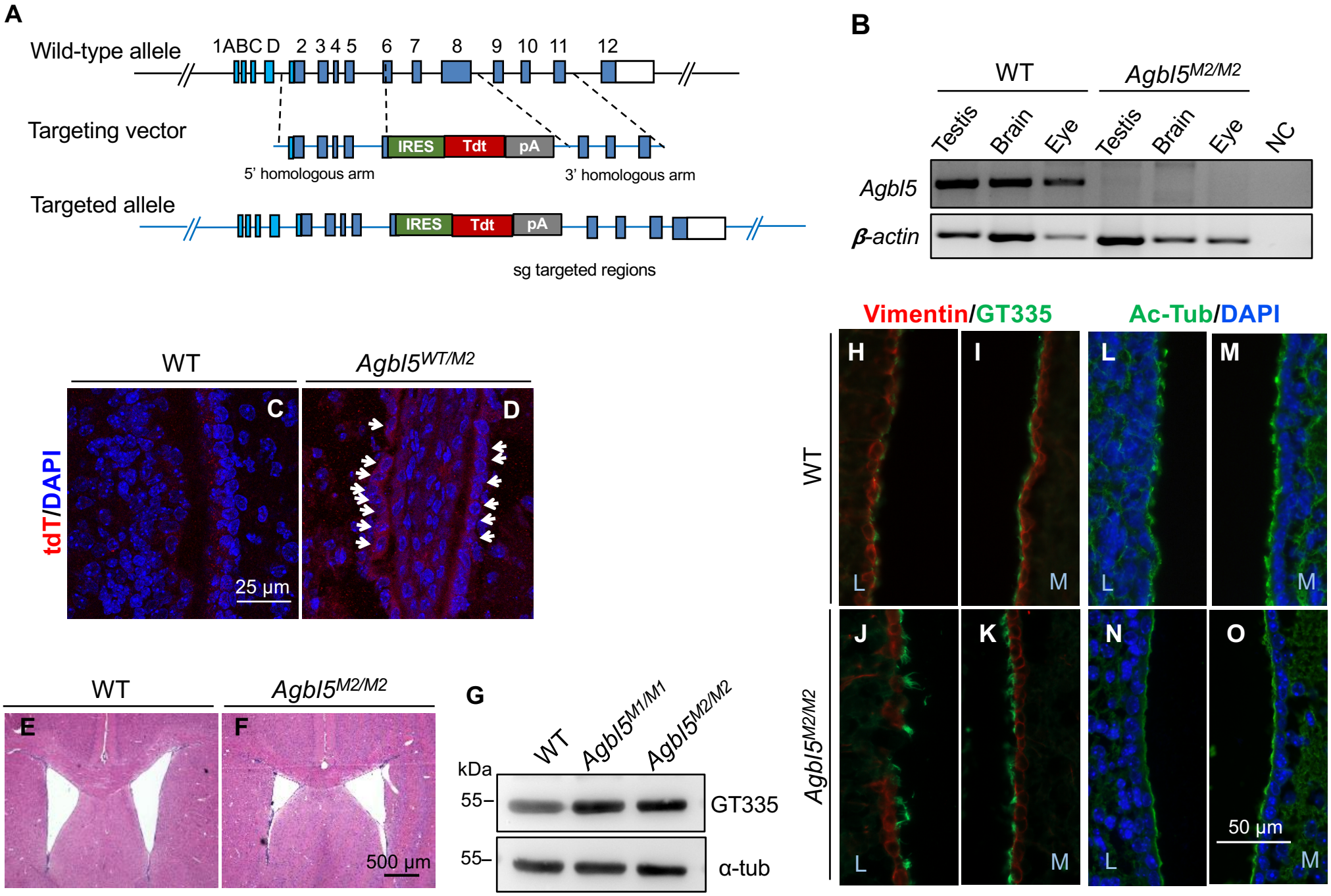
A
Wild-type allele
1ABC D 2 3 4 5 6 7 8 9 10 11 12
Targeting vector
IRES
Tdt
pA
5' homologous arm
3' homologous arm
Targeted allele
sg targeted regions
B
WT
Agbl5M2/M2
Testis
Brain
Eye
Testis
Brain
Eye
NC
Agbl5
β-actin
WT
Agbl5WT/M2
tdT/DAPI
C
D
25 μm
WT
Agbl5M2/M2
E
F
500 μm
G
kDa
WT
Agbl5M1/M1
Agbl5M2/M2
55–
GT335
55–
α-tub
Vimentin/GT335
Ac-Tub/DAPI
WT
Agbl5M2/M2
H
I
L
M
J
K
N
O
50 μm